

Gamma-Ray Burst Afterglows in Pulsar-Wind Bubbles

Arieh Königl¹ and Jonathan Granot²

¹Department of Astronomy & Astrophysics and Enrico Fermi Institute, University of Chicago, 5640 S. Ellis Ave., Chicago, IL 60637; arieh@jets.uchicago.edu

²Institute for Advanced Study, Olden Lane, Princeton, NJ 08540; granot@ias.edu

ABSTRACT

We propose to identify pulsar-wind bubbles (PWBs) as the environment in which the afterglow emission in at least some gamma-ray burst (GRB) sources originates. Such bubbles could naturally account for both the high fraction of the internal energy residing in relativistic electrons and positrons (ϵ_e) and the high magnetic-to-internal energy ratio (ϵ_B) that have been inferred in a number of sources from an interpretation of the afterglow emission as synchrotron radiation. GRBs might occur within PWBs under a number of scenarios: in particular, in the supranova model of GRB formation a prolonged (months to years) period of intense pulsar-type wind from the GRB progenitor precedes the burst. Focusing on this scenario, we construct a simple model of the early-time structure of a plerionic supernova remnant (SNR), guided by recent results on the Crab and Vela SNRs. The model is based on the assumption of an “equipartition” upper bound on the electromagnetic-to-thermal pressure ratio in the bubble and takes into account synchrotron-radiation cooling. We argue that the effective upstream hydrogen number density for a relativistic shock propagating into the bubble is given by $n_{\text{H,equiv}} = [4p + (B' + \mathcal{E}')^2/4\pi]/m_p c^2$, where B' and \mathcal{E}' are, respectively, the comoving magnetic and electric fields and p is the particle pressure. We show that, for plausible parameter values, $n_{\text{H,equiv}}$ spans the range inferred from spectral fits to GRB afterglows and that its radial profile varies within the bubble and may resemble a uniform interstellar medium or a stellar wind. We consider how the standard expressions for the characteristic synchrotron spectral quantities are modified when the afterglow-emitting shock propagates inside a PWB instead of in a uniform interstellar medium and demonstrate that the predictions for the empirically inferred values of ϵ_e and ϵ_B are compatible with the observations. Finally, we outline a self-consistent interpretation of the X-ray emission features detected in sources like GRB 991216 in the context of the supranova/PWB picture.

Subject headings: gamma rays: bursts — MHD — pulsars: general — pulsars: individual (Crab Nebula, Vela Pulsar) — shock waves — supernova remnants

1. Introduction

Gamma-ray burst (GRB) sources are commonly interpreted in terms of nonthermally emitting shocks associated with relativistic (and possibly highly collimated) outflows from stellar-mass black holes or strongly magnetized and rapidly rotating neutron stars (see, e.g., Piran 1999 and Mészáros 2001 for reviews). The prompt high-energy emission is thought to originate in the outflow itself, with the γ -rays attributed to internal shocks within the flow and with the associated optical “flash” and radio “flare” emission ascribed to the reverse shock that is driven into the outflowing material as it starts to be decelerated by the inertia of the swept-up ambient gas. By contrast, the longer-term, lower-energy afterglow emission (see, e.g., van Paradijs, Kouveliotou, & Wijers 2000 for a review) is attributed to the forward shock that propagates into the ambient medium. The ambient gas is usually taken to be either the interstellar medium (ISM) of the host galaxy or a stellar wind from the GRB progenitor star.

It appears that most of the observed emission from GRBs and their afterglows represents synchrotron radiation (e.g., Sari, Piran, & Narayan 1998; Panaitescu & Mészáros 1998; Sari & Piran 1999; Chevalier & Li 2000; Lloyd & Petrosian 2000). In view of source-energetics considerations, the emission efficiency must be high. This implies that the ratio ϵ_e of the internal energy in relativistic electrons and positrons to the total internal energy density in the emission region is not much smaller than 1, and that the ratio ϵ_B of the magnetic-to-internal energy densities is not much smaller than ϵ_e . If the shocked gas consists of protons and electrons, then only moderately high ($\lesssim 0.1$) values of ϵ_e may be expected even under optimal circumstances (e.g., Bykov & Mészáros 1996; Pohl & Schlickeiser 2000). For ϵ_e to approach 1, it is probably necessary for the preshock gas to be composed primarily of e^\pm pairs. A pair-dominated outflow is, in fact, a feature of certain GRB models (e.g., Usov 1994; Mészáros & Rees 1997; Grimsrud & Wasserman 1998). Furthermore, the radiative efficiency of the reverse shock (and possibly also of the forward shock during the early afterglow phase) could be enhanced through pair creation by the high-energy photons comprising the gamma-ray pulse (e.g., Thompson & Madau 2000; Mészáros, Ramirez-Ruiz, & Rees 2001). There is, however, no natural way to account for large values of ϵ_e during the later phases of afterglows in a typical ISM or stellar-wind environment.

It is in principle also possible to account for comparatively large values of ϵ_B in internal and reverse shocks by appealing to shock compression of magnetized outflows (e.g., Spruit, Daigne, & Drenkhahn 2001; Granot & Königl 2001, hereafter GK). However, in the case of afterglows in the standard scenario, the highest values of ϵ_B that might be attained in this fashion (e.g., in a shock propagating into a magnetized wind from a progenitor star; see

Biermann & Cassinelli 1993) could at best account only for the low end of the actual range inferred in GRB afterglows ($\epsilon_B \gtrsim 10^{-5}$; e.g., Panaitescu & Kumar 2002). For example, one could not explain in this way the estimate $\epsilon_B \sim 0.01 - 0.1$ (derived by model fitting of one of the most comprehensive spectral data sets obtained to date) in the GRB 970508 afterglow (e.g., Wijers & Galama 1999; Granot, Piran, & Sari 1999; Chevalier & Li 2000).¹

As an alternative to compressional amplification of a preshock field, various proposals have been advanced for generating strong magnetic fields in the shocks themselves, but it is still unclear whether any of them can naturally account for a source like GRB 970508. For example, Medvedev & Loeb (1999) suggested that a two-stream instability behind the shock can generate fields that fluctuate on the very short scale of the plasma skin depth. However, the most likely value of ϵ_B predicted by this scheme is rather low ($\ll 0.01$), as is also the value of ϵ_e (e.g., Pohl & Schlickeiser 2000); furthermore, questions have been raised about whether the fields will not, in fact, be damped on a similar microscopic scale (Gruzinov 1999). Thompson & Madau (2000) suggested that acceleration of the preshock gas by the prompt gamma-ray pulse photons would induce shearing motions that could significantly amplify the ambient magnetic field. It is, however, unlikely that the preshock optical depth would be large enough for this effect to play a role for the comparatively large spatial scales ($\gtrsim 10^{17}$ cm) and low preshock densities ($\sim 0.03 - 3$ cm⁻³) inferred for the GRB 970508 afterglow (see Mészáros et al. 2001). Blandford (2000), arguing by analogy with supernovae like Cas A, proposed that the afterglow emission in a source like GRB 970508 arises near the contact discontinuity that separates the swept-up ambient gas from the outflowing matter, where these two components can mix and interact. The large inferred magnetic field presumably originates in the central source and undergoes additional amplification in the turbulent interaction zone, but a quantitative model of this scenario has not yet been presented.²

In this paper we propose that the large values of ϵ_B and ϵ_e inferred in afterglows like GRB 970508 arise naturally if the outflow that gives rise to the gamma-ray pulse

¹The inferred value of ϵ_e in this source is also fairly high ($\sim 0.1 - 0.6$).

²A related idea was discussed by Smolsky & Usov (2000), who considered a magnetized, pulsar-type wind and suggested that it does not initially form a forward shock but rather that the oscillating currents in the wind front excite large-amplitude electromagnetic waves in the ambient medium and that high-energy electrons accelerated in the front radiate in the field of these waves. However, these authors still attributed afterglow emission detected more than a day after the gamma-ray pulse (as was the case for GRB 970508) to a conventional forward shock that develops ahead of the wind front by that time. Additional ideas on how large-amplitude electromagnetic waves in Poynting flux-dominated outflows could lead to large values of ϵ_B in afterglows were outlined by Lyutikov & Blackman (2001).

expands into a pulsar-wind bubble (PWB). Such a bubble forms when the relativistic wind (consisting of relativistic particles and magnetic fields) that emanates from a pulsar shocks against the ambient gas and creates a “pulsar nebula,” whose structure is analogous to that of a stellar wind-inflated “interstellar bubble.” When a bubble of this type expands inside a supernova remnant (SNR), it gives rise to a “plerionic” SNR, of which the Crab and Vela remnants are prime examples (see, e.g., Chevalier 1998 for a review). GRBs can arise inside PWBs under a number of plausible scenarios, some of which have already been considered in the literature. For example, Gallant & Achterberg (1999) suggested that, if GRB outflows are formed in neutron-star binary mergers and expand into PWBs created by the progenitor pulsars, then acceleration of relativistic ions in the nebula by the forward shock could in principle account for the observed population of ultra-high-energy cosmic rays (UHECRs).³ Vietri & Stella (1998, 1999) presented a scenario for the origin of GRBs in which a rotationally supported “supramassive” neutron star (SMNS) forms either by a supernova explosion that is triggered by the collapse of a massive star or as a result of mass transfer in a low-mass X-ray binary (LMXB). In this picture, the neutron star loses angular momentum (and associated centrifugal support) through a pulsar-type wind until (on a time scale of several months to several years) it becomes unstable to collapse to a black hole (a process that, in turn, induces a GRB outflow). Vietri & Stella (1998, hereafter VS) noted the analogy between the proposed “supranova” remnants and plerionic SNRs, but they did not explicitly address the structure of SMNS wind nebulae and their implications to GRB afterglows.⁴ The afterglow sources observed to date are associated with “long” bursts (of duration $\gtrsim 2$ s) and are often found within the projected image of the host galaxy. Such sources could plausibly arise in the collapse of (or the merger of a compact object with) a massive star (e.g., Woosley 2000), although an LMXB progenitor may also be consistent with the data (Vietri & Stella 1999). In view of the evidence that at least some afterglow sources are located along the line of sight to a star-forming region (e.g., Mészáros 2001),

³The association of UHECRs with GRBs was originally proposed by Waxman (1995), Milgrom & Usov (1995), and Vietri (1995). Some difficulties with the simplest formulation of this idea were recently discussed by Stecker (2000) and Farrar & Piran (2000). UHECRs may, however, originate in winds from young, rapidly spinning and strongly magnetized neutron stars even if the latter are not linked to GRBs (see Blasi, Epstein, & Olinto 2000).

⁴In a recent paper, Inoue, Guetta, & Pacini 2001 discussed some observational consequences of the precursor plerion in the supranova scenario as well as the prospects for its direct detection. Their picture differs from ours in that they assume that the PWB disrupts and penetrates through the supernova ejecta shell, attaining a size that is about an order of magnitude larger than the SNR radius, and they associate the afterglow-emitting gas with entrained SNR fragments or the ambient ISM. By contrast, in our picture the PWB remains largely confined within the SNR shell, and the afterglow emission arises in the high-effective-density interior gas.

we adopt the supranova version of the SMNS scenario (VS) as the underlying framework for our discussion.⁵ In §2 we estimate the physical parameters of SMNS winds and of supranova remnants in light of recent work on plerions, and we then model the structure of the resulting PWBs. In §3 we consider the expected properties of GRB afterglows that originate in such an environment. Our conclusions are summarized in §4.

2. Pulsar-Wind Bubbles in Young Supernova Remnants

2.1. The Supranova Scenario

Supramassive neutron stars are general-relativistic equilibrium configurations of rapidly rotating neutron stars whose masses exceed the maximum mass of a nonrotating neutron star (e.g., Cook, Shapiro, & Teukolsky 1994; Salgado et al. 1994). A uniformly rotating SMNS that loses energy and angular momentum adiabatically while conserving its total baryon mass follows an evolutionary sequence that brings it to a point where it becomes unstable to axisymmetric perturbations, whereupon it undergoes a catastrophic collapse to a black hole. In their supranova model, VS postulated that the SMNS, which forms in the course of a supernova explosion of a massive star, is magnetized and loses energy and angular momentum through a pulsar-type wind.⁶ The rate of energy loss can be estimated from the magnetic dipole-radiation formula

$$L_w = \frac{B_*^2 R_*^6 \Omega_*^4}{6c^3} = 7.0 \times 10^{44} \left(\frac{B_*}{10^{12} \text{ G}} \right)^2 \left(\frac{R_*}{15 \text{ km}} \right)^6 \left(\frac{\Omega_*}{10^4 \text{ s}^{-1}} \right)^4 \text{ ergs s}^{-1}, \quad (1)$$

where B_* is the polar surface magnetic field, R_* is the circumferential radius (neglecting the distinction between its equatorial and polar values in this approximation), and Ω_* is the (uniform) angular velocity (whose maximum value is $\sim 2 \times 10^4 \text{ s}^{-1}$; e.g., Haensel,

⁵It has not yet been explicitly demonstrated that the supranova scenario can account for long bursts; in fact, it has even been suggested (Böttcher & Fryer 2001) that this model is most likely to produce short bursts. We note, however, that long bursts could in principle be generated in the course of the collapse of the SMNS to a black hole (see Kluźniak & Ruderman 1998). Alternatively, if (as suggested by VS) the GRB outflow is produced after the collapse in a magnetized debris disk formed by the outer layers of the SMNS, then a long duration could be a consequence of a comparatively low disk viscosity (see, e.g., Popham, Woosley, & Fryer 1999 and Ruffert & Janka 1999) or of a magnetically mediated spin-up torque exerted by the black hole (van Putten & Ostriker 2001).

⁶As noted by VS, gravitational radiation, possibly associated with the excitation of r modes in the SMNS (e.g., Andersson 1998), is an alternative loss mechanism. However, in view of the uncertainties involved in quantifying this process, we follow VS and neglect it in the ensuing discussion.

Lasota, & Zdzunik 1999).⁷ The magnetic field amplitude in this estimate is normalized by the typical radio-pulsar value. This situation is to be distinguished from scenarios in which a magnetized rotator with a much stronger field ($\gtrsim 10^{15}$ G) is invoked to account for the GRB outflow itself (e.g., Usov 1994; Thompson 1994; Blackman & Yi 1998; Kluźniak & Ruderman 1998; Spruit 1999; Ruderman, Tao, & Kluźniak 2000). The initial neutron-star magnetic field might be amplified to such strengths by differential rotation (e.g., Kluźniak & Ruderman 1998⁸) or through dynamo action (e.g., Thompson & Duncan 1993⁹). For the comparatively low field amplitudes adopted in the supranova scenario, the dynamical effect of the magnetic field on the SMNS structure should be negligible (see, e.g., Bocquet et al. 1995).

The wind power L_w consists of electromagnetic and particle contributions. The magnetic field is expected to have a dominant toroidal component, which scales with distance r from the center as $1/r$. Under ideal-MHD conditions, the Poynting-to-particle energy flux ratio in the wind is given by

$$\sigma_w = \frac{B_w^2}{4\pi\rho_w c^2}, \quad (2)$$

where B_w is the field amplitude and ρ_w is the rest-mass density (both measured in the fluid frame), and it remains constant along the flow after the terminal speed is reached. There has been a great deal of debate in the literature about the value of σ_w in relativistic pulsar outflows and about whether an ideal-MHD description is appropriate (see, e.g., Arons 1998 and Chiueh, Li, & Begelman 1998 for discussions of this topic). For example, dynamical and radiative models of the Crab pulsar nebula have yielded preshock values of σ_w in the range $\sim 2 - 5 \times 10^{-3}$ (e.g., Arons 2002).¹⁰ On the other hand, recent X-ray observations

⁷The magnetic dipole luminosity also scales as $\sin^2\theta_{\Omega B}$, where $\theta_{\Omega B}$ is the angle between the rotation and dipole axes. However, as the spin-down torque of radio pulsars is evidently largely independent of the value of $\theta_{\Omega B}$ (e.g., Bhattacharya & Srinivasan 1995), we did not include this factor in equation (1).

⁸These authors also mention the possibility, suggested independently by VS in their outline of the supranova scenario, that differential rotation leading to a very strong field and possibly a GRB outflow could be induced in an SMNS when it starts to collapse after losing centrifugal support.

⁹These authors associate the dynamo action with neutrino flux-driven convection, which should occur if the stellar spin period $2\pi/\Omega$ is shorter than the convective overturn time $\sim 10^{-3}F_{39}^{-1/3}$ s at the base of the convection zone, where F_{39} is the neutrino heat flux in units of 10^{39} ergs cm^{-2} s^{-1} , the expected value for a typical supernova explosion. Since the energy released in a supranova explosion may be significantly larger than in a typical supernova, and since the neutron-star mass is also higher in this case, the neutrino flux could be similarly larger and the convection condition might not be satisfied, which would be consistent with the assumption that the SMNS magnetic field does not exceed typical pulsar values.

¹⁰Begelman (1998), however, argued that a key underlying assumption of some of the dynamical estimates

of the Vela pulsar nebula have been interpreted as implying $\sigma_w \sim 1$ (Helfand, Gotthelf, & Halpern 2001).¹¹ In view of this uncertainty, and in order to examine the dependence of our model results on this parameter, we derive solutions for σ_w in the range $10^{-3} - 1$.

We also need to specify the Lorentz factor γ_w and the composition of the outflow. Spectral (e.g., Kennel & Coroniti 1984) and optical brightness-distribution (Gallant & Arons 1994) models of the Crab nebula have implied a current value of $\sim 3 \times 10^6$ for γ_w upstream of the shock. However, although these fits account for the optical-through-gamma-ray observations, they do not explain the measured radio spectrum. In a recent model, Atoyan (1999) interpreted the latter as being produced by a relic population of relativistic electrons that had been accelerated during the early years of the pulsar and that have subsequently lost most of their energy by radiation and adiabatic-expansion losses. Based on this interpretation, he argued that the Crab pulsar was born with a period of $\sim 3 - 5$ ms (as compared with previous estimates of ~ 19 ms)¹² and initially had $\gamma_w \leq 10^4$. In light of this result, we adopt $\gamma_w = 10^4$ as a fiducial value in our calculations: we assume that its magnitude is roughly the same in all objects and that it does not change significantly over the SMNS spin-down time. The pulsar outflow could consist of e^\pm pairs as well as ions. In fact, by modeling the wind termination shock in the Crab nebula, Gallant & Arons (1994) inferred that the energy flux in ions is approximately twice that in pairs in that source, and we already mentioned (see §1) the suggestion by Gallant & Achterberg (1999) that UHECRs might be identified with heavy ions in GRB-associated PWBs. Nevertheless, for simplicity, we assume in our model that the SMNS wind is composed purely of e^\pm pairs.¹³ In this case the wind power can be written as

$$L_w = 4\pi(1 + \sigma_w)r^2n_w(r)\gamma_w^2\beta_w m_e c^3, \quad (3)$$

where $n_w(r)$ is the fluid-frame wind particle density at a radius r , m_e is the electron mass,

— that the magnetic field inside the shocked-wind bubble maintains a coherent, large-scale, toroidal structure — may not be valid, and he suggested that σ_w could be higher in this source.

¹¹This interpretation was, however, questioned by Arons (2002), who suggested that σ_w in the Vela nebula is, instead, < 0.05 ; an even lower upper limit was given by Chevalier (2000), who proposed that $\sigma_w < 10^{-4}$ in this source.

¹²Independent arguments for why radio pulsars like the Crab and Vela were likely born with rotation periods $\lesssim 1$ ms were recently given by Lai, Chernoff, & Cordes (2001) in the context of an interpretation of the apparent alignment of the spin axes, proper motion directions, and polarization vectors of the Crab and Vela pulsars.

¹³If the ion and pair energy fluxes are indeed comparable and these two components do not exchange energy efficiently, then the resulting bubbles would be approximated by the weakly cooling PWB solutions presented in §2.3.

and $\beta_w c$ is the wind speed.¹⁴

The spin-down time of a rapidly rotating SMNS can be estimated as

$$t_{\text{sd}} = \frac{\Delta E_{\text{rot}}}{L_w} \approx 6 \left(\frac{\alpha}{0.5} \right) \left(\frac{M_*}{2.5 M_\odot} \right)^2 \left(\frac{R_*}{15 \text{ km}} \right)^{-6} \left(\frac{\Omega_*}{10^4 \text{ s}^{-1}} \right)^{-3} \left(\frac{B_*}{10^{12} \text{ G}} \right)^{-2} \text{ yr} \quad (4)$$

(see VS), where $\Delta E_{\text{rot}} = \alpha G M_*^2 \Omega_* / 2c$ is the portion of the rotational energy of an SMNS of mass M_* and angular velocity Ω_* that needs to be lost before it becomes unstable to collapse.¹⁵ The basic time scale is determined by the underlying physical picture of a magnetized neutron star in which a significant fraction of the binding energy is invested in rotation (which is uniform, and thus does not lead to field amplification much above typical pulsar values). However, the expected variations in the parameter values that appear in equation (4) could cause t_{sd} to range between a few months and a few years. It is instructive to compare these values with Atoyan’s (1999) estimate (obtained from a fit to the Crab radio data) of the initial spin-down time of the Crab pulsar, $t_{\text{sd}} \leq 30 \text{ yr}$ (a factor $\gtrsim 20$ smaller than previous estimates that assumed a fixed functional dependence of the spin-down torque on Ω). The similarity of these estimates is consistent with the possibility that the same modeling framework may apply to both plerionic SNRs and SMNS-driven bubbles.

Atoyan (1999) suggested that the initial rotation energy of the Crab pulsar was comparable to that of the supernova explosion that produced it, and noted that his inferred value of E_{rot} ($\gtrsim 10^{51}$ ergs) was consistent with independent arguments (Chevalier 1977) that the Crab nebula had originated in a normal Type II supernova event. In the case of an SMNS it is, however, unlikely that the explosion energy is as large as the initial rotation energy ($\sim 10^{53}$ ergs), but since the energy (ΔE_{rot}) deposited in the PWB is evidently of the same order as E_{rot} , the supernova ejecta (subscript **ej**) would be accelerated by the expanding bubble and one could obtain an approximate equality between E_{rot} and $E_{\text{ej}} = 0.5 M_{\text{ej}} v_{\text{ej}}^2$. For typical ejecta mass $\gtrsim 10 M_\odot$, this would imply $v_{\text{ej}} \approx 0.1 c$ at $t = t_{\text{sd}}$ (about an order of magnitude higher than in a typical SNR). This estimate of v_{ej} (which agrees with that of VS) is supported by measurements of X-ray emission (e.g., Piro et al. 2000) and absorption (e.g., Lazzati et al. 2001) features in some GRB sources (see §3.2).

In the supranova scenario, the GRB is associated with the collapse of the SMNS, which occurs at a time t_{sd} after the supernova explosion. Unless the explosion takes place within

¹⁴In view of the large estimated value of γ_w , we henceforth set β_w equal to 1 in all numerical expressions.

¹⁵The total rotational energy of the SMNS is given by $E_{\text{rot}} = j G M_*^2 \Omega_* / 2c$, where the parameter j measures the stellar angular momentum in units of $G M_*^2 / c$ and has values in the range 0.57–0.78 for realistic equations of state (e.g., Cook et al. 1994; Salgado et al. 1994).

a dense molecular cloud, the mass of the swept-up ambient medium will remain negligible in comparison with M_{ej} over this time scale and will not affect the SNR dynamics. To simplify the treatment, we assume that this is the case.¹⁶ The expanding PWB is expected to compress the ejecta into a thin shell and accelerate it (e.g., Reynolds & Chevalier 1984). To within factors of order 1, the outer radius of the bubble at time t_{sd} can be approximated by the product of $v_b \equiv v_{\text{ej}}(t_{\text{sd}})$ times the SMNS spin-down time:

$$R_b = v_b t_{\text{sd}} = 9.5 \times 10^{16} \beta_{b,-1} \tau_{\text{sd}} \text{ cm} , \quad (5)$$

where we set $v_b/c \equiv \beta_b = 0.1\beta_{b,-1}$ and $t_{\text{sd}} = \tau_{\text{sd}} \text{ yr}$. To the extent that $v_b \propto (\Delta E_{\text{rot}}/M_{\text{ej}})^{1/2}$ has nearly the same value in all sources, the magnitude of R_b is determined by that of t_{sd} . In a similar vein, if the energy $\Delta E_{\text{rot}} = 10^{53} \Delta E_{53}$ ergs lost during the SMNS lifetime is approximately constant from source to source ($\Delta E_{53} \sim 1$), then t_{sd} can also be used to parameterize the SMNS wind power: $L_w = \Delta E_{\text{rot}}/t_{\text{sd}} = 3.2 \times 10^{45} \Delta E_{53}/\tau_{\text{sd}} \text{ ergs s}^{-1}$.

In their original proposal, VS focused on the expected effect of the supranova ejecta and SMNS energy release on the baryon content of the environment in which the GRB occurs. This was motivated by the general requirement (see, e.g., Piran 1999) that the burst energy be channeled into a region with a relatively low number of massive particles in order for the outflow to attain the high ($\gtrsim 10^2$) Lorentz factors inferred in GRBs. However, this property of the GRB outflow is probably determined primarily by the generic properties of the central object (e.g., Mészáros & Rees 1997; Kluźniak & Ruderman 1998; Vlahakis & Königl 2001) rather than by the matter-sweeping action of the ejecta and SMNS wind. Instead of this aspect of the supranova scenario, we emphasize here the favorable consequences of the expected delay between the supranova explosion and the GRB event to the creation of PWBs in which afterglows with high inferred values of ϵ_B and ϵ_e could naturally arise.¹⁷

¹⁶As a further simplification, we neglect the possible incorporation of mass from the ejecta shell into the bubble interior through evaporation by the “hot” shocked-wind material. This effect, which has been considered in the study of interstellar bubbles (e.g., Weaver et al. 1977), would be strongly suppressed if the magnetic field were strictly transverse to the flow direction, as is assumed in our model. However, even a small mean radial field component might lead to a thermal conductivity that is high enough to significantly affect the mass budget inside the bubble.

¹⁷Another potential implication of this delay, which we consider in §3.2, involves the interpretation of the X-ray spectral features detected in some GRB sources.

2.2. Wind-Bubble Structure

We follow previous treatments of PWB structure (Rees & Gunn 1974; Kennel & Coroniti 1984; Emmering & Chevalier 1987) in our assumptions about the basic morphology of the bubble: we take it to be spherical, with an outer radius R_b , and assume that the pulsar wind propagates freely (with $\sigma_w = \text{const}$) until it is shocked at a radius R_s . Our model differs, however, from previous treatments in that we take account of nonthermal radiation losses (which could be important during the early phase of the nebula) and we do not assume that ideal MHD is necessarily applicable throughout the shocked-wind bubble. As has been demonstrated in the previously cited papers, a PWB that expands adiabatically with a nonrelativistic speed and that contains a large-scale toroidal magnetic field frozen into the matter corresponds to $\sigma_w \approx \beta_b \ll 1$. Such a model thus cannot describe a bubble with $\beta_b \ll 1$ and $\sigma_w \lesssim 1$.¹⁸ If $\sigma_w \sim 1$, then the postshock flow is magnetically dominated from the start. But even if $\sigma_w \ll 1$ and the postshock value of the fluid-frame magnetic-to-particle pressure ratio p_B/p is < 1 , this ratio will grow with radius r in the bubble and, if radiative cooling is even moderately important and flux freezing continues to hold, its value will at some point increase above 1 and could eventually become $\gg 1$. However, as was already argued by Rees & Gunn (1974), a situation in which p_B significantly exceeds p is unlikely to persist in a real PWB. We therefore adopt an alternative formulation and drop the assumption of ideal MHD in the shocked gas at the point where the electromagnetic pressure first rises above the particle pressure. We assume, instead, that beyond that point the electromagnetic pressure in the bubble remains in approximate equipartition with the particle pressure.¹⁹ For definiteness, we assume that the flow obeys ideal MHD within the wind shock and we fix the electromagnetic-to-particle pressure ratio $\delta \equiv (\mathcal{E}'^2 + B'^2)/8\pi p$ in the bubble by setting

$$\delta = \text{const} = \max\{\delta_{\text{ps}}, 1\}, \quad \max\{R_s, R_{\text{eq}}\} \leq r \leq R_b. \quad (6)$$

Here \mathcal{E}' and B' are, respectively, the fluid-frame electric and magnetic fields, the subscript **ps** denotes postshock quantities, and R_{eq} is the radius where p_B/p first increases to 1 (assuming ideal-MHD evolution) if $\delta_{\text{ps}} < 1$. According to this prescription, when the

¹⁸The presence of a large-scale toroidal magnetic field also implies that the bubble will become elongated and will assume a cylindrical, rather than a spherical, shape (see Begelman & Li 1992). We return to the question of the bubble morphology in §3.2.

¹⁹An equipartition assumption (between the thermal and magnetic pressure components) was previously incorporated as a limiting case in the (Newtonian) plerion evolutionary model of Reynolds & Chevalier (1984). Possible physical mechanisms for the breakdown of ideal MHD when p_B increases to p were discussed by Kennel, Gedalin, & Lominadze (1988), Begelman (1998), and Salvati et al. (1998).

postshock value of δ is less than 1 ($\delta_{\text{ps}} < 1$), the bubble flow starts out maintaining flux freezing, but if p_B/p increases to 1 before the outer boundary is reached, it switches to a nonideal evolution (with δ fixed at 1) beyond R_{eq} . If, however, σ_w is large enough that $\delta_{\text{ps}} \geq 1$, then the entire PWB volume is subject to the equipartition constraint, with δ fixed at δ_{ps} . For a strong shock, the postshock value of δ can be expressed as a function of the wind magnetization parameter σ_w and speed β_w .²⁰ Specifically,

$$\delta_{\text{ps}} = \frac{B'_{\text{ps}}{}^2}{8\pi p_{\text{ps}}} = \frac{4\gamma_{\text{ps}}^2\beta_{\text{ps}}^2 + 1}{2\sigma_w^{-1}\gamma_{\text{ps}}^2\beta_{\text{ps}}^2 - 1 + (\gamma_{\text{ps}}\beta_{\text{ps}}/\gamma_w\beta_w)^2}, \quad (7)$$

where $\gamma_{\text{ps}} \equiv (1 - \beta_{\text{ps}}^2)^{-1/2}$ is the Lorentz factor of the postshock flow and β_{ps} is given by the solution of the equation

$$\beta_{\text{ps}}^3 - \frac{\beta_w(4 + 5\sigma_w + 2\sigma_w\gamma_w^{-2}\beta_w^{-2})}{3(\sigma_w + 1)}\beta_{\text{ps}}^2 + \frac{\beta_{\text{ps}}}{3} + \frac{\beta_w\sigma_w}{3(\sigma_w + 1)} = 0. \quad (8)$$

In the limit $\gamma_w \gg 1$, both δ_{ps} and β_{ps} become functions of σ_w alone (see GK): equation (7) simplifies to

$$\delta_{\text{ps}} = \frac{B'_{\text{ps}}{}^2}{8\pi p_{\text{ps}}} = \frac{4\gamma_{\text{ps}}^2\beta_{\text{ps}}^2 + 1}{2\sigma_w^{-1}\gamma_{\text{ps}}^2\beta_{\text{ps}}^2 - 1}, \quad (9)$$

whereas the equation for β_{ps} is reduced from a cubic to a quadratic, with the solution

$$\beta_{\text{ps}} = \frac{1 + 2\sigma_w + [16\sigma_w(1 + \sigma_w) + 1]^{1/2}}{6(1 + \sigma_w)}. \quad (10)$$

For $\sigma_w = 10^{-3}, 10^{-2}, 0.1$, and 1, these expressions yield $\{\beta_{\text{ps}}, \delta_{\text{ps}}\} = \{0.33, 0.006\}$, $\{0.35, 0.059\}$, $\{0.43, 0.53\}$ and $\{0.73, 4.37\}$, respectively. Note that, for $\sigma_w \leq 0.2$ (corresponding to $\beta_{\text{ps}} \leq 0.5$), δ_{ps} is ≤ 1 , so that (by eq. [6]) $\delta = 1$.

We simplify the treatment of the bubble interior by assuming that the flow is purely radial, that [in spherical coordinates (r, θ, ϕ)] the magnetic field continues to possess only a ϕ component ($\mathbf{B} = B\hat{\phi}$; see Begelman 1998) and the electric field only a θ component ($\mathcal{E} = \mathcal{E}\hat{\theta}$; this follows from the previous two assumptions when ideal MHD is applicable, but needs to be postulated when it is not), and that the only nonzero spatial derivatives are in the radial direction. Under these assumptions, the particle number, energy, and momentum

²⁰In typical applications, the speed of the wind shock is much lower than that of the wind, and even than v_b (see Emmering & Chevalier 1987). For the sake of simplicity, we therefore set it equal to zero and identify the rest frame of the wind shock with that of the source.

conservation equations in the PWB take the form

$$\frac{1}{c} \frac{\partial}{\partial t} (\gamma n) + \frac{1}{r^2} \frac{\partial}{\partial r} (r^2 \gamma \beta n) = 0, \quad (11)$$

$$\frac{1}{c} \frac{\partial}{\partial t} \left(\gamma^2 w - p + \frac{\mathcal{E}^2 + B^2}{8\pi} \right) + \frac{1}{r^2} \frac{\partial}{\partial r} \left[r^2 \left(\gamma^2 \beta w + \frac{\mathcal{E} B}{4\pi} \right) \right] = -\frac{\gamma \Lambda}{c}, \quad (12)$$

$$\frac{1}{c} \frac{\partial}{\partial t} \left(\gamma^2 \beta w + \frac{\mathcal{E} B}{4\pi} \right) + \frac{1}{r^2} \frac{\partial}{\partial r} \left[r^2 \left(\gamma^2 \beta^2 w + \frac{\mathcal{E}^2 + B^2}{8\pi} \right) \right] + \frac{\partial p}{\partial r} = -\frac{\gamma \beta \Lambda}{c}, \quad (13)$$

where n is the particle number density, $w = \rho c^2 + e + p$ is the enthalpy density (with e being the internal energy density and ρ the rest-mass density), Λ is the emissivity (which, like the preceding quantities, is measured in the fluid rest frame), β is the radial speed in units of c , and γ is the Lorentz factor. The electric and magnetic field amplitudes in these equations are measured in the central-source frame; they are related to their fluid-frame counterparts through the Lorentz transformations

$$\mathcal{E}' = \gamma(\mathcal{E} - \beta B), \quad B' = \gamma(B - \beta \mathcal{E}). \quad (14)$$

The evolution of \mathcal{E} is governed by Faraday's law,

$$\frac{1}{c} \frac{\partial B}{\partial t} + \frac{1}{r} \frac{\partial}{\partial r} (r \mathcal{E}) = 0. \quad (15)$$

Given that $\gamma_w \gg 1$, the shocked gas should be well described by a relativistic equation of state

$$p = \frac{e}{3} = \frac{w}{4}. \quad (16)$$

The acoustic speed v_{ac} would be correspondingly high. For example, in the ideal-MHD regime, where it is given by $[(1/3 + \delta/2)/(1 + \delta/2)]^{1/2} c$ (representing the phase speed of the fast-magnetosonic wave; e.g., Königl 1980), $v_{\text{ac}}/c \approx 0.75$ for $\delta \approx 1$, which we take to be large enough in comparison with β_b (≈ 0.1) to justify a steady-state approximation within the bubble. We therefore set $\partial/\partial t = 0$ in equations (11)–(15). Equation (11) then yields

$$r^2 \gamma \beta n = R_s^2 \gamma_{\text{ps}} \beta_{\text{ps}} n_{\text{ps}} \equiv C. \quad (17)$$

The constant C can be evaluated from the shock jump condition

$$\gamma_{\text{ps}} \beta_{\text{ps}} n_{\text{ps}} = \gamma_w \beta_w n_w, \quad (18)$$

where we have assumed that there is no pair production at the wind shock. Using also equation (3), one obtains

$$C = \frac{L_w}{4\pi(1 + \sigma_w) \gamma_w m_e c^3}. \quad (19)$$

Under the steady-state assumption, equation (15) implies that $\mathcal{E}(r) \propto 1/r$ inside the PWB. Normalizing to the value immediately behind the shock, we infer

$$\mathcal{E}(r) = \frac{\mathcal{E}_{\text{ps}} R_{\text{ps}}}{r} = \left(\frac{\sigma_w}{1 + \sigma_w} \frac{\beta_w L_w}{c} \right)^{1/2} \frac{1}{r}. \quad (20)$$

Elimination of the radiative cooling term from equations (12) and (13) leads to

$$\frac{dp}{dr} + \gamma^2 \beta w \frac{d\beta}{dr} + \frac{B - \beta \mathcal{E}}{4\pi r} \frac{d}{dr}(rB) = 0, \quad (21)$$

whereas subtraction of $\gamma\beta$ times equation (13) from γ times equation (12) yields

$$\frac{1}{r^2} \frac{d}{dr}(r^2 \gamma \beta w) - \gamma \beta \frac{dp}{dr} + \frac{\gamma(\mathcal{E} - \beta B)}{4\pi r} \frac{d}{dr}(rB) = -\frac{\Lambda}{c} \quad (22)$$

(the entropy equation), where in both cases we took account of the constancy of the product $r\mathcal{E}$ inside the bubble. If σ_w is not $\ll 1$, then most of the bubble volume will be in the equipartition regime ($\delta \approx 1$, or, equivalently, $\epsilon_B \approx \epsilon_e$), in which case Λ will typically be dominated by synchrotron radiation.²¹ To simplify the treatment, we take synchrotron emission to be the main radiative cooling process even for low values of σ_w . Furthermore, we assume that at any given location within the bubble the e^\pm pairs have a monoenergetic energy distribution characterized by a random (or “thermal”) Lorentz factor γ_e . The latter approximation is appropriate if the postshock gas undergoes significant radiative cooling (e.g., Granot, Piran, & Sari 2000), which, as we discuss in §2.3, may be the case in SMNS-driven bubbles. The synchrotron emissivity can then be written in the form

$$\Lambda = \frac{4}{3} \sigma_T c n \gamma_e^2 \frac{B'^2}{8\pi}, \quad (23)$$

where σ_T is the Thomson cross section. In view of equation (16), it is then also possible to write the particle pressure as

$$p = \frac{1}{3} \gamma_e n m_e c^2. \quad (24)$$

Combining this expression with equation (17) gives

$$\gamma_e = Dr^2 \gamma \beta p, \quad (25)$$

²¹In the equipartition region, synchrotron self-Compton emission cannot exceed the synchrotron radiation under any circumstances: it is comparable to the synchrotron emission if the bubble is highly radiative, but it remains much smaller if the radiative cooling time is longer than the bubble expansion time.

where $D \equiv 3/m_e c^2 C = 3/\gamma_{\text{ps}} \beta_{\text{ps}} n_{\text{ps}} R_s^2 m_e c^2$. Using equations (14), (19), (24), and (25) in equation (23), one can express the radiative cooling term in equation (22) in the form

$$\frac{\Lambda}{c} = G \gamma^3 \beta (rB - \beta r \mathcal{E})^2 p^2, \quad (26)$$

where $G \equiv (\sigma_T/2\pi m_e c^2) D = 6\sigma_T(1 + \sigma_w)\gamma_w/m_e c L_w$.

We now consider the term rB that appears in equations (21), (22), and (26). Its form depends on whether the flow is in the ideal-MHD or the equipartition regime of the bubble interior. The ideal-MHD case corresponds to setting $\mathcal{E}' = 0$ in equation (14), which implies $rB = r\mathcal{E}/\beta \propto 1/\beta$ (by eq. [20]). It is then straightforward to obtain from equations (21) and (22) (after also substituting $w = 4p$ from eq. [16]) the following pair of coupled, first-order, ordinary differential equations for the variables β and p , which give the structure of the ideal-MHD sector of the PWB:

$$\frac{d\beta}{dr} = \left[Gr^2 \mathcal{E}^2 p^2 + 8\gamma^2 \beta^2 \frac{p}{r} \right] \left[4\gamma^4 \beta (3\beta^2 - 1)p - \frac{3}{4\pi} \frac{\mathcal{E}^2}{\beta} \right]^{-1}, \quad R_s \leq r \leq \min\{R_{\text{eq}}, R_{\text{b}}\}, \quad (27)$$

$$\frac{dp}{dr} = \left[4\gamma^2 \beta^2 p - \frac{\mathcal{E}^2}{4\pi\gamma^2\beta^2} \right] \left[Gr^2 \mathcal{E}^2 p^2 + 8\gamma^2 \beta^2 \frac{p}{r} \right] \left[\frac{3}{4\pi} \mathcal{E}^2 + 4\gamma^4 \beta^2 (1 - 3\beta^2)p \right]^{-1} \\ R_s \leq r \leq \min\{R_{\text{eq}}, R_{\text{b}}\}, \quad (28)$$

with \mathcal{E} given by equation (20).

For the nonideal (equipartition) regime, we combine equations (6) and (14) to obtain a quadratic equation for rB , whose relevant root is

$$rB_{\text{eq}} = \frac{2\beta}{1 + \beta^2} r\mathcal{E} + \frac{[8\pi\delta\gamma^2(1 + \beta^2)r^2p - r^2\mathcal{E}^2]^{1/2}}{\gamma^2(1 + \beta^2)}. \quad (29)$$

Using this relation as well as equations (16), (20), and (26) in equations (21) and (22), it is once again possible to extract explicit differential equations for β and p :

$$\frac{d\beta}{dr} = \left\{ \left[1 + \frac{\delta(rB_{\text{eq}} - \beta r\mathcal{E})}{\gamma^2[(1 + \beta^2)rB_{\text{eq}} - 2\beta r\mathcal{E}]} \right] G\gamma^2\beta(rB_{\text{eq}} - \beta r\mathcal{E})^2 p^2 + \left[8\beta + \frac{2\delta r\mathcal{E}}{\gamma^4[(1 + \beta^2)rB_{\text{eq}} - 2\beta r\mathcal{E}]} \right] \frac{p}{r} \right\} \left\{ 4[\gamma^2(3\beta^2 - 1) - \delta]p + \frac{(r^2\mathcal{E}B_{\text{eq}} - 8\pi\delta\gamma^2\beta r^2p)[4\beta rB_{\text{eq}} - (1 + 3\beta^2)r\mathcal{E}]}{2\pi(1 + \beta^2)\gamma^2[(1 + \beta^2)rB_{\text{eq}} - 2\beta r\mathcal{E}]r^2} \right\}^{-1}, \\ \max\{R_s, R_{\text{eq}}\} \leq r \leq R_{\text{b}}, \quad (30)$$

$$\frac{dp}{dr} = \left\{ 1 + \frac{\delta(rB_{\text{eq}} - \beta r\mathcal{E})}{\gamma^2[(1 + \beta^2)rB_{\text{eq}} - 2\beta r\mathcal{E}]} \right\}^{-1} \times \\ \times \left\{ \left[\frac{(\beta r\mathcal{E} - rB_{\text{eq}})(r^2\mathcal{E}B_{\text{eq}} - 8\pi\delta\gamma^2\beta r^2 p)}{2\pi(1 + \beta^2)\gamma^2[(1 + \beta^2)rB_{\text{eq}} - 2\beta r\mathcal{E}]r^2} - 4\gamma^2\beta p \right] \left(\frac{d\beta}{dr} \right) + \frac{2\delta(\beta r\mathcal{E} - rB_{\text{eq}})}{\gamma^2[(1 + \beta^2)rB_{\text{eq}} - 2\beta r\mathcal{E}]} \frac{p}{r} \right\}, \\ \max\{R_s, R_{\text{eq}}\} \leq r \leq R_b, \quad (31)$$

where the term $(d\beta/dr)$ in equation (31) is given by the expression (30). Equations (27)–(31) are integrated over their respective validity domains subject to the boundary conditions

$$\beta(R_s) = \beta_{\text{ps}}, \quad p(R_s) = p_{\text{ps}}, \quad (32)$$

where β_{ps} is given by equation (10) and the postshock pressure

$$p_{\text{ps}} = \frac{\sigma_w \gamma_w^2 \beta_w^2 n_w(R_s) m_e c^2}{2\delta_{\text{ps}} \gamma_{\text{ps}}^2 \beta_{\text{ps}}^2} \quad (33)$$

(with $n_w(r)$ given by eq. [3]) is similarly obtained from the wind-shock jump conditions (see GK). The value of R_s , where the boundary conditions (32) are imposed, is not known a priori and must be determined from an additional constraint. This can be provided by requiring global particle conservation: for a bubble considered at time t after the supernova explosion, the total number of particles within the radius $R_b(t)$ [which consists of the unshocked wind at $r < R_s(t)$ and the shocked wind at $r > R_s(t)$] is equal to the total number of particles injected by the central neutron star over the time t . The pair injection rate at the source is given by

$$\dot{N} = \frac{L_w}{(1 + \sigma_w)\gamma_w m_e c^2}, \quad (34)$$

and hence the total number of particles within R_b at time t is $N(t) = \dot{N}t$. We approximate $t \approx R_b/\beta_b c$, which should be accurate to within a factor of order 1 (for example, $t = 1.5R_b/\beta_b c$ in the case of an adiabatic bubble, with the numerical coefficient decreasing in the presence of cooling; see Reynolds & Chevalier 1984). The number of particles within the volume occupied by the unshocked wind is thus

$$N(r < R_s) = \dot{N} \frac{R_s}{\beta_w c} \approx N(t) \frac{R_s}{ct} \approx \beta_b N \frac{R_s}{R_b}, \quad (35)$$

whereas the total number of particles within the shocked-wind region is

$$N(R_s < r < R_b) = \int_{R_s}^{R_b} 4\pi r^2 \gamma n dr = \frac{\beta_b N}{R_b} \int_{R_s}^{R_b} \frac{dr}{\beta}, \quad (36)$$

where we used equations (5), (17), (19), and (34). The solutions obtained in this manner will not, in general, be entirely self-consistent, since the bubble structure evolves with time

whereas we have assumed a steady state. The wind gas cannot arrive at $r = R_b$ at the speed v_b after traveling from the origin for the same duration (viz., the age of the bubble) as the ejecta that is currently at R_b , given that the wind speed is $> v_b$ everywhere within this region and that the ejecta speed was $< v_b$ before it reached R_b . This argument implies that, if the particle-conservation condition is imposed, then $\beta(R_b)$ will be lower than (rather than exactly match) β_b . This is not a serious inconsistency, since the flow near R_b will generally be highly subsonic and therefore can readily adjust to match the speed (v_b) of the outer boundary. Nevertheless, in order to assess the sensitivity of the results to the choice of the imposed constraint, we also solve the system of equations subject to the alternative condition $\beta(R_b) = \beta_b$.

2.3. Illustrative Solutions

The governing equations can be rendered dimensionless by introducing $\tilde{r} \equiv r/R_b$ (with \tilde{r}_s and \tilde{r}_{eq} denoting the dimensionless counterparts of R_s and R_{eq} , respectively) as well as $\tilde{B} \equiv B/\mathcal{E}(R_b)$ and $\tilde{p} \equiv p/p_{\text{ref}}$, where

$$p_{\text{ref}} \equiv \frac{\mathcal{E}^2(R_b)}{8\pi} = \left(\frac{2\sigma_w}{1 + \sigma_w} \right) \left(\frac{\beta_w L_w}{16\pi R_b^2 c} \right) \equiv \left(\frac{2\sigma_w}{1 + \sigma_w} \right) p_1, \quad (37)$$

(see eq. [20]).²² They then take the form

$$\frac{d\beta}{d\tilde{r}} = \left[\frac{3a}{8\pi} \tilde{p}^2 + 4\gamma^2 \beta^2 \frac{\tilde{p}}{\tilde{r}} \right] \left[2\gamma^4 \beta (3\beta^2 - 1) \tilde{p} - \frac{3}{\beta \tilde{r}^2} \right]^{-1}, \quad \tilde{r}_s \leq \tilde{r} \leq \min\{\tilde{r}_\delta, 1\}, \quad (38)$$

$$\begin{aligned} \frac{d\tilde{p}}{d\tilde{r}} &= \left[4\gamma^2 \beta^2 \tilde{p} - \frac{2}{\gamma^2 \beta^2 \tilde{r}^2} \right] \left[\frac{3a}{8\pi} \tilde{p}^2 + 4\gamma^2 \beta^2 \frac{\tilde{p}}{\tilde{r}} \right] \times \\ &\times \left[\frac{3}{\tilde{r}^2} + 2\gamma^4 \beta^2 (1 - 3\beta^2) \tilde{p} \right]^{-1}, \quad \tilde{r}_s \leq \tilde{r} \leq \min\{\tilde{r}_\delta, 1\}, \end{aligned} \quad (39)$$

$$\tilde{r} \tilde{B}_{\text{eq}} = \frac{2\gamma^2 \beta + [\delta \gamma^2 (1 + \beta^2) \tilde{r}^2 \tilde{p} - 1]^{1/2}}{\gamma^2 (1 + \beta^2)}, \quad (40)$$

$$\frac{d\beta}{d\tilde{r}} = \left\{ \left[1 + \frac{\delta(\tilde{r} \tilde{B}_{\text{eq}} - \beta)}{\gamma^2 [(1 + \beta^2) \tilde{r} \tilde{B}_{\text{eq}} - 2\beta]} \right] \frac{3a}{16\pi} \gamma^2 \beta (\tilde{r} \tilde{B}_{\text{eq}} - \beta)^2 \tilde{p}^2 + \right.$$

²²The parameter p_1 is defined so as to isolate the σ_w -independent part of p_{ref} : it is equal to p_{ref} evaluated at $\sigma_w = 1$.

$$\begin{aligned}
& + \left[2\beta + \frac{\delta}{2\gamma^4[(1+\beta^2)\tilde{r}\tilde{B}_{\text{eq}} - 2\beta]} \right] \frac{\tilde{p}}{\tilde{r}} \left\{ [\gamma^2(3\beta^2 - 1) - \delta] \tilde{p} + \right. \\
& \left. + \frac{(\tilde{r}\tilde{B}_{\text{eq}} - \delta\gamma^2\beta\tilde{r}^2\tilde{p})(4\beta\tilde{r}\tilde{B}_{\text{eq}} - 1 - 3\beta^2)}{(1+\beta^2)\gamma^2[(1+\beta^2)\tilde{r}\tilde{B}_{\text{eq}} - 2\beta]\tilde{r}^2} \right\}^{-1}, \\
& \max\{\tilde{r}_s, \tilde{r}_\delta\} \leq \tilde{r} \leq 1,
\end{aligned} \tag{41}$$

$$\begin{aligned}
\frac{d\tilde{p}}{d\tilde{r}} &= \left\{ 1 + \frac{\delta(\tilde{r}\tilde{B}_{\text{eq}} - \beta)}{\gamma^2[(1+\beta^2)\tilde{r}\tilde{B}_{\text{eq}} - 2\beta]} \right\}^{-1} \times \\
& \times \left\{ 4 \left[\frac{(\beta - \tilde{r}\tilde{B}_{\text{eq}})(\tilde{r}\tilde{B}_{\text{eq}} - \delta\gamma^2\beta\tilde{r}^2\tilde{p})}{(1+\beta^2)\gamma^2[(1+\beta^2)\tilde{r}\tilde{B}_{\text{eq}} - 2\beta]\tilde{r}^2} - \gamma^2\beta\tilde{p} \right] \left(\frac{d\beta}{d\tilde{r}} \right) + \frac{2\delta(\beta - \tilde{r}\tilde{B}_{\text{eq}})}{\gamma^2[(1+\beta^2)\tilde{r}\tilde{B}_{\text{eq}} - 2\beta]} \frac{\tilde{p}}{\tilde{r}} \right\}, \\
& \max\{\tilde{r}_s, \tilde{r}_\delta\} \leq \tilde{r} \leq 1,
\end{aligned} \tag{42}$$

(corresponding to eqs. [27]–[31], respectively), where

$$a \equiv \left[\frac{\sigma_T L_w}{(1+\sigma_w)m_e c^3 R_b} \right] (\sigma_w \beta_w)^2 \gamma_w \equiv \left(\frac{2\sigma_w^2}{1+\sigma_w} \right) a_1. \tag{43}$$

The parameter a_1 in equation (43) was introduced so as to isolate the σ_w -independent part of the parameter a : it is equal to a evaluated at $\sigma_w = 1$.²³ As we explicitly demonstrate below, a_1 measures the relative importance of radiative cooling within the bubble. Numerically, $1/a_1$ is of the order of the nominal radiative cooling time of the bubble in units of R_b/c , and hence the larger the value of a_1 , the stronger the role that radiative cooling plays in determining the bubble structure. In the supranova model, if β_b and ΔE_{rot} are approximately constant from source to source, then a_1 scales with the bubble age t_{sd} at the time of the GRB as roughly t_{sd}^{-2} (see eqs. [4] and [5]).

The boundary conditions given by equation (32) are applied at \tilde{r}_s , which, in turn, is given either by the relation

$$\frac{\beta_b}{1 - \beta_b \tilde{r}_s} \int_{\tilde{r}_s}^1 \frac{d\tilde{r}}{\beta(\tilde{r})} = 1 \tag{44}$$

(see eqs. [34]–[36]) or by imposing the condition

$$\beta(\tilde{r} = 1) = \beta_b \tag{45}$$

We solve this system of equations for given choices of the parameter σ_w and a_1 by iterating on the value of \tilde{r}_s until both the boundary conditions (32) and the constraint (44) or (45) are satisfied.

²³Note that the term in square parentheses in the expression for a can be interpreted as a “bubble compactness parameter,” using the terminology often employed in studies of compact astrophysical pair configurations.

Once the values of $\beta(\tilde{r})$ and $\tilde{p}(\tilde{r})$ are known, they may be used to obtain the other physical quantities of interest. In particular,

$$n(\tilde{r}) = \left[\frac{4p_1}{(1 + \sigma_w)\beta_w\gamma_w m_e c^2} \right] \frac{1}{\gamma(\tilde{r})\beta(\tilde{r})\tilde{r}^2}, \quad (46)$$

$$\frac{\gamma_e(\tilde{r})}{\gamma_w} = \left(\frac{3\sigma_w\beta_w}{2} \right) \tilde{r}^2 \gamma(\tilde{r})\beta(\tilde{r})\tilde{p}(\tilde{r}). \quad (47)$$

The postshock value of n is given from equations (10 and (18) and can, in turn, be used with equations (24) and (33) to yield the postshock value of γ_e ,

$$\frac{\gamma_{e,ps}}{\gamma_w} = \frac{3\beta_w \left\{ 2\gamma_{ps}^2\beta_{ps}^2 - \sigma_w [1 - (\gamma_{ps}\beta_{ps}/\gamma_w\beta_w)^2] \right\}}{2(4\gamma_{ps}^2\beta_{ps}^2 + 1)\gamma_{ps}\beta_{ps}}. \quad (48)$$

Furthermore, $\tilde{B}(\tilde{r})$ is given by $1/\tilde{r}\beta(\tilde{r})$ in the ideal-MHD zone and by equation (40) in the equipartition region. We will also find it useful to consider the variable

$$\psi \equiv \frac{(\mathcal{E}' + B')^2}{8\pi p}, \quad (49)$$

which is equal to p_B/p in the ideal-MHD regime. Note that the ideal-MHD sector of the PWB corresponds to the region where $\psi(\tilde{r})$ is < 1 and that, within this sector, $\psi = \delta$.

Figure 1 shows $\tilde{r}_s = R_s/R_b$, the ratio of the wind-shock radius to the outer bubble radius, as a function of the cooling parameter a_1 for the two alternative constraints (N conservation and $\beta(R_b) = \beta_b$) discussed in §2.2. Results are shown for $\sigma_w = 1, 0.1, 10^{-2}$, and 10^{-3} . According to our adopted scalings, $R_b \propto \tau_{sd} \propto a_1^{-1/2}$, so R_b decreases with increasing a_1 . It is, however, seen that when cooling becomes important, the relative width of the bubble, $1 - \tilde{r}_s$, also decreases with increasing a_1 . This can be attributed to the decrease in the internal thermal pressure brought about by the cooling: a lower pressure, in turn, requires a shorter length scale to achieve the needed pressure gradient for decelerating the flow. For given values of a_1 and σ_w , \tilde{r}_s is larger when the terminal speed is fixed than when particle conservation is enforced. This can be attributed to the fact that, in the former case, the gas speed between $r = R_s$ and $r = R_b$ decreases from β_{ps} (eq. [10]) to β_b , whereas in the latter case it decreases from β_{ps} to $\beta(R_b) < \beta_b$ (see discussion at the end of §2.2): the larger velocity decrement evidently requires a longer deceleration length ($R_b - R_s$). Figure 1 also depicts the a_1 dependence of $\tilde{r}_{eq} = R_{eq}/R_b$, the normalized equipartition radius (where p_B/p first increases to 1 if $\delta_{ps} < 1$). It shows that, whereas the $\sigma_w = 1$ solution obeys nonideal MHD throughout the shocked-wind bubble (since $\delta_{ps} > 1$ in this case), the nonideal regime becomes progressively smaller with decreasing σ_w . This is a direct consequence of equation (9), which indicates that δ_{ps} scales approximately linearly

with σ_w : the lower the value of δ_{ps} , the longer it will take for p_B/p in the postshock flow to rise above 1 (our condition for the termination of the ideal-MHD regime). The relative extent of the ideal-MHD region is larger for the fixed- $\beta(R_b)$ solutions, so much so that the solutions of this type with the two lowest values of σ_w contain no nonideal-MHD zone. This can be understood from the systematically higher values of $\beta(\tilde{r})$ (see Figs. 2 and 3) and correspondingly lower values of $\tilde{B}(\tilde{r}) \propto 1/\tilde{r}\beta(\tilde{r})$ and hence of $p_B(\tilde{r})/p(\tilde{r})$ in the fixed- $\beta(R_b)$ solutions in comparison with their N -conserving counterparts.

Figures 2 and 3 exhibit the \tilde{r} dependence of various quantities of interest in PWB solutions obtained by imposing the N -conservation and fixed- $\beta(R_b)$ constraints, respectively, for the same 4 values of the wind magnetization parameter as in Figure 1 (spanning 3 orders of magnitude in σ_w) and for 5 values of the cooling parameter (spanning 4 orders of magnitude in a_1). If $\beta_{b,-1}$ and ΔE_{53} are both set equal to 1, then the chosen values of a_1 ($= 0.45, 5.04, 45.3, 504,$ and 4539) correspond to SMNS spin-down times $t_{\text{sd}} = 100, 30, 10, 3$ and 1 yr, respectively. Bubbles with a_1 near the lower end of this range resemble adiabatic PWBs, whereas configurations with a_1 near the upper range are highly radiative. Radio pulsars have inferred surface magnetic fields in the range $\sim 10^{12} - 10^{13}$ G, so, by equation (4), a variation of roughly two orders of magnitude in the value of t_{sd} is naturally expected.

The upper panels in Figures 2 and 3 show the behavior of $\beta(\tilde{r})$. The *dashed* lines in these panels indicate the postshock (β_{ps}) and outer-boundary (β_b) speeds, whereas the *dash-dotted* curves depict the purely adiabatic ($a_1 = 0$) solutions. The displayed results confirm that $\beta(R_b) < \beta_b$ in the N -conserving solutions. The greatest discrepancy between $\beta(R_b)$ and the actual speed (β_b) of the outer boundary occurs for $\sigma_w = 1$, in which case $\beta(R_b)/\beta_b$ decreases from ~ 0.13 to ~ 0.0063 as a_1 increases from 0.1 to 10^3 . We consider this to be a tolerable discrepancy, given (as we already noted in §2.2) that the flow near $\tilde{r} = 1$ is highly subsonic. The $\beta(\tilde{r})$ curves further demonstrate that the values of β in the N -conserving solutions are lower than those in the corresponding $\beta(R_b) = \beta_b$ solutions also for all other values of \tilde{r} where the respective solutions overlap. The lower values of β lead (on account of the particle flux-conservation relation [11]) to systematically higher values of n in the N -conserving solutions (see the second row of panels in Figs. 2 and 3). The radial profiles of n are nearly flat for low values of the cooling parameter, but when radiative effects are important and contribute to the compression, $n(\tilde{r})$ rises monotonically between \tilde{r}_s and $\tilde{r} = 1$ with a slope that is steeper (particularly in the nonideal-MHD regime) the larger the value of a_1 .

The third row of panels in Figures 2 and 3 displays $\gamma_e(\tilde{r})/\gamma_w$. The *dashed* line marks the postshock value of this quantity, and the *dash-dotted* curves again represent the purely

adiabatic case. The random Lorentz factor declines monotonically with \tilde{r} in the $\sigma_w = 1$ and 0.1 solutions, but at lower values of σ_w (for which the electromagnetic pressure contribution is small) and so long as cooling remains relatively unimportant ($a_1 \lesssim 10$), $\gamma_e(\tilde{r})$ initially increases behind the wind shock to make it possible to attain the necessary total pressure. The minimum value of $\gamma_e(\tilde{r})$ (reached at $\tilde{r} = 1$) decreases (as expected) with increasing a_1 and is lower for the N -conserving solutions than for the fixed- $\beta(R_b)$ ones. This difference can be understood from the fact that the particle density near the outer boundary is lower in the latter case [corresponding to a higher value of $\beta(\tilde{r} = 1)$], so γ_e must be larger to bring the pressure up to its requisite value.

Of particular relevance to the evolution of GRB afterglows is the behavior of the thermal and electromagnetic pressures. The radial profiles of p (normalized by p_1) are shown in the fourth row of panels in Figures 2 and 3. It is seen that the behavior of $p(\tilde{r})$ varies with the parameter choices and that the details depend on the nature of the constraint imposed on the solution. For $\sigma_w = 1$, the curves decline monotonically when cooling is relatively unimportant but increase monotonically at high values of a_1 . For $\sigma_w = 0.1$, the curves decrease monotonically for all plotted values of the cooling parameter, whereas for $\sigma_w = 10^{-3}$ in the fixed- $\beta(R_b)$ solution they increase monotonically for all exhibited values of a_1 . In the remaining cases, the curves increase with \tilde{r} near the inner boundary of the bubble and decrease near its outer boundary. Since $p \propto \gamma_e n$, one can understand the shape of the curves by comparing them with the corresponding curves in the second and third rows of panels. One finds that, quite generally, the behavior of p is dominated by that of γ_e for low values of a_1 , but that the influence of the density variations becomes progressively more important as the cooling parameter increases.

The effect of the electromagnetic fields can be inferred from the behavior of the variable ψ and of the ratio \mathcal{E}'/B' , shown in the bottom two rows of panels in Figures 2 and 3. Note that one can write $\psi = \delta + \mathcal{E}'B'/4\pi p$ (see eq. [49]). Immediately behind the wind shock (in which, by construction, $\mathcal{E}' = 0$), ψ is equal to δ_{ps} (given by eq. [9]). If $\delta_{\text{ps}} \geq 1$ then the nonideal-MHD regime starts right there: beyond that point, δ remains fixed at its postshock value but ψ and \mathcal{E}'/B' increase with \tilde{r} . If $\delta_{\text{ps}} < 1$, then the evolution proceeds under ideal-MHD conditions ($\mathcal{E}' = 0$), with ψ continuing to coincide with δ (which in this regime equals p_B/p) up to the point where it reaches 1. This point marks the end of the ideal-MHD regime and corresponds to \tilde{r}_{eq} . Beyond \tilde{r}_{eq} , ψ continues to increase monotonically with \tilde{r} (and now so does also \mathcal{E}'/B'), but δ remains fixed at 1 (see eq. [6]). The figures show that, as expected, the electromagnetic contribution to the total pressure becomes progressively larger as σ_w increases, and they further demonstrate that \mathcal{E}'/B' exhibits a similar trend. It is also seen that cooling enhances the relative importance of the electromagnetic fields, which can be understood from the fact that it reduces the magnitude

of the thermal pressure component. The overall behavior of ψ and \mathcal{E}'/B' does not appear to depend strongly on the choice of constraint under which the solution is obtained, although the corresponding curves in the two figures differ in their details (see also the related discussion in connection with Fig. 1 above). As we show in §3.1, the variable ψ plays a key role in the modeling of relativistic shocks that propagate inside a PWB.

3. Implications to GRB Afterglows

3.1. Emission-Region Parameters

Pulsar wind-inflated bubbles, such as those predicted to arise prior to the onset of the high-energy burst in the supranova scenario, provide an optimal environment for GRB afterglows since they naturally yield high electron and magnetic energy fractions (ϵ_e and ϵ_B) behind the propagating shock wave that gives rise to the afterglow emission. High values of ϵ_e are expected from the fact that relativistic pulsar-type winds are likely dominated by an electron-positron component, whereas significant values of ϵ_B should naturally occur if the winds are characterized by a high magnetization parameter.

The observationally inferred values of ϵ_e and ϵ_B are derived from spectral fits that are based on the standard model assumptions of a “cold,” weakly magnetized proton-electron preshock medium. We now consider what would be the “equivalent” values (which we denote by the subscript *equiv*) that one would derive if the afterglow-emitting shock propagated instead inside a PWB. The postshock quantities can be determined from the appropriate generalizations of the expressions presented in §2.2, taking account of the fact that the preshock gas is now “hot” (with $w = 4p$; eq. [16]) rather than “cold” and that it may contain a nonzero comoving electric field. One imposes the continuity of the energy flux $\gamma^2\beta w + \mathcal{E}B/4\pi$, momentum flux $\gamma^2\beta^2 w + p + (\mathcal{E}^2 + B^2)/8\pi$, and tangential electric field \mathcal{E} in the frame of the shock. The possible presence of a nonzero \mathcal{E}' requires the specification of an additional shock jump condition, which we take to be the conservation of magnetic flux during the fluid’s transit through the shock. On the assumption that the field is transverse to the shock propagation direction, this condition translates into the requirement that βB be continuous in the shock frame. Combining these constraints, one obtains a cubic equation for the postshock (subscript 2) flow speed (measured in the shock frame) that is akin to the expression (8). In the limit of an ultrarelativistic shock, the latter again reduces to a quadratic equation, whose relevant solution is

$$\beta_2 = \frac{1 + \psi + [(1 + \psi)^2 + 3(2 + \psi)\psi]^{1/2}}{3(2 + \psi)}, \quad (50)$$

where ψ is defined by equation (49). Equation (50) reproduces equation (10) if one substitutes $2\sigma_w$ for ψ : this is consistent with the fact that $\psi/2$ becomes equal to the magnetization parameter $\sigma \equiv \mathcal{E}B/4\pi\gamma^2\beta w$ of the preshock medium in the limit $\beta \rightarrow 1$ and $w \rightarrow 4p$.²⁴

By substituting $\mathcal{E} = \gamma(\mathcal{E}' + \beta B')$ and $B = \gamma(B' + \beta\mathcal{E}')$ (see eq. [14]) into the expressions for the energy and momentum fluxes in the shock frame, one finds that, if the shock is highly relativistic (so that the upstream β is close to 1 in the frame of the shock), the upstream fluxes have the same forms as in a purely hydrodynamic shock if w in the latter is replaced by $w + (B' + \mathcal{E}')^2/4\pi$. Shock models of GRB afterglows traditionally infer an ambient gas density by assuming that a hydrodynamic shock propagates into a standard ISM or stellar-wind environment with an enthalpy density $w = n_{\text{H}}m_p c^2$, where m_p is the proton mass. This motivates us to define the “equivalent” hydrogen number density

$$n_{\text{H,equiv}} \equiv \frac{1}{m_p c^2} \left[w + \frac{(B' + \mathcal{E}')^2}{4\pi} \right], \quad (51)$$

which under the assumption of a relativistic equation of state can be written as $n_{\text{H,equiv}} = 4(1 + \psi/2)p/m_p c^2$. This quantity is plotted in the top row of panels in Figures 4 and 5 as a function of \tilde{r} for each of the model PWBs presented in §2.3. These figures also show (in the second row of panels) plots of the radial dependence of $k \equiv -d \log n_{\text{H,equiv}}/d \log r$, the effective power-law index of the equivalent hydrogen density distribution. Our model assumption of an abrupt transition between the ideal- and nonideal-MHD regimes at \tilde{r}_{eq} introduces an unphysical discontinuity in the value of k at this point: the displayed curves have been smoothed at this location by interpolation across the discontinuity.

To simplify the discussion, we restrict attention to the three synchrotron-spectrum characteristics considered by Sari et al. (1998, hereafter SPN), namely, the break frequencies ν_m and ν_c and the peak flux $F_{\nu,\text{max}}$; we refer the reader to that paper for the definition of these quantities and for the derivation of the standard expressions for emission by a

²⁴An indirect measure of the value of the magnetization parameter just ahead of the afterglow-producing shock is possibly provided by the power-law index p of the synchrotron-emitting particle energy distribution, which can be deduced from the shape of the observed spectrum (e.g., Sari, Piran, & Narayan 1998). Kirk et al. (2000) argued that an ultrarelativistic, unmagnetized shock that accelerates particles in a “cold” medium through the first-order Fermi process produces a “universal” power law of index $p \approx 2.2$, and that this value increases with the preshock magnetization (so that, for example, $p \approx 2.3$ for $\sigma = 0.01$, assuming $\mathcal{E}' = 0$). The often-quoted “canonical” value of p for GRB afterglows is 2.5, although in some sources a significantly higher value has been inferred (e.g., Huang, Dai, & Lu 2000; Panaitescu & Kumar 2002—note, however, that the latter reference also lists a few sources in which $p < 2.2$ has been deduced).

spherical shock in which there is no pair production. In the interest of simplicity, we also assume that the equivalent hydrogen number density inside the bubble is roughly constant; as the $n_{\text{H,equiv}}$ plots in Figures 4 and 5 demonstrate, this approximation is usually adequate over the bulk of the bubble volume, especially when the cooling is not too strong. We distinguish between two cases: weakly cooling PWBs (corresponding to cooling parameters $a_1 \lesssim 10^2$, or, for our fiducial values, $\tau_{\text{sd}} \gtrsim 10$), whose radial widths $\Delta R_b \equiv (R_b - R_s)$ are of the order of R_b , and strongly cooling PWBs ($a_1 \gg 10^2$, $\tau_{\text{sd}} \ll 10$), for which $\Delta R_b/R_b \ll 1$. In the weakly cooling case, one can approximate the volume of the shocked bubble gas by that of the sphere that is bounded by the shock.

In the standard case of a uniform ambient medium and a slow-cooling (adiabatic) shock, one can express the two break frequencies and the peak flux in terms of the shock energy E , the ambient density n_{H} , the observed time t , as well as ϵ_e , ϵ_B , and the distance to the source (see eq. [11] in SPN). In particular, $\nu_m \propto \epsilon_e^2 \epsilon_B^{1/2} E^{1/2} t^{-3/2}$, $\nu_c \propto \epsilon_B^{-3/2} E^{-1/2} n_{\text{H}}^{-1} t^{-1/2}$, and $F_{\nu,\text{max}} \propto \epsilon_B^{1/2} E n_{\text{H}}^{1/2}$. In the case of a shock propagating inside a weakly cooling PWB, it turns out that the above expressions for ν_m and ν_c are reproduced if n_{H} , ϵ_e , and ϵ_B are everywhere replaced by $n_{\text{H,equiv}}$ (eq. [51]),

$$\epsilon_{e,\text{equiv}} \equiv \frac{m_e \gamma_e}{m_p \gamma_{21}} \epsilon_e = \left(\frac{m_e}{m_p} \right) \left(\frac{1 + \beta_2}{\beta_2} \right) \left(\frac{4\gamma_2^2 \beta_2^2 - \psi}{4\gamma_2^2 \beta_2^2 + 1} \right) \epsilon_e \gamma_e, \quad (52)$$

and

$$\epsilon_{B,\text{equiv}} \equiv \frac{B_2'^2}{32\pi\gamma_{21}^2 n_{\text{H,equiv}} m_p c^2} = \left(\frac{1 + \beta_2}{4\beta_2} \right)^2 \left(\frac{1}{2} + \frac{1}{\psi} \right)^{-1}, \quad (53)$$

respectively, where γ_2 is the Lorentz factor corresponding to β_2 , γ_{21} is the Lorentz factor of the postshock fluid in the stationary frame (evaluated again on the assumption that the afterglow-emitting shock is highly relativistic), and γ_e is given by equation (47). In deriving equation (52), we have made use of equation (24) and of the continuity of the particle flux $\gamma\beta n$ in the shock frame. The expression for $F_{\nu,\text{max}}$ is reproduced by making similar substitutions and then multiplying by the factor

$$F_{\text{correct}} = \frac{n}{n_{\text{H,equiv}}} = \frac{3}{4} \frac{m_p}{m_e} \left(1 + \frac{\psi}{2} \right)^{-1} \gamma_e^{-1}. \quad (54)$$

The functions $\epsilon_{e,\text{equiv}}(\tilde{r})$, $\epsilon_{B,\text{equiv}}(\tilde{r})$, and $F_{\text{correct}}(\tilde{r})$ are plotted in the third-through-fifth rows, respectively, of Figures 4 and 5, with the *dashed* line in each panel marking the value of the respective quantity immediately behind the pulsar-wind shock. Although the underlying expressions were obtained under the assumption of a weakly cooling bubble, it turns out (see next paragraph) that they continue to apply also in the strongly cooling case. The values of $\epsilon_{e,\text{equiv}}$ were calculated by setting $\epsilon_e = 1$ in equation (52)—consistent

with our PWB model approximation of a pure- e^\pm wind. Inasmuch as F_{correct} does not differ from 1 by more than a factor of a few over most of the explored parameter range, it can be concluded that the standard expressions will remain approximately applicable if one simply replaces n_{H} , ϵ_e , and ϵ_B by their “equivalent” counterparts. The derived values of F_{correct} also verify that $n_{\text{H,equiv}}$ is usually much greater than $(m_e/m_p)n$, consistent with the PWB model assumption of a “hot” equation of state.

To derive the corresponding expressions for a strongly cooling PWB, one can approximate the bubble as a thin shell of radius $\sim R_b$. The bubble volume traversed by a shock that is located at a distance x from the inner radius of the bubble is then $V(x) \approx 4\pi R_b^2 x$. Relating x to the observed time t and to the Lorentz factor Γ of the shocked gas by $x \approx 4\Gamma^2 t$, following SPN,²⁵ and setting $E \approx V\Gamma^2 n_{\text{H,equiv}} m_p c^2$ in the adiabatic-shock case, one finds that the standard expressions (eq. [11] in SPN) continue to apply if one makes the aforementioned substitutions for ϵ_e , ϵ_B , and n_{H} , and, in addition, multiplies the expressions for ν_m and ν_c by A_{correct} and $1/A_{\text{correct}}$, respectively, where

$$A_{\text{correct}} = \left(\frac{4Et}{17\pi c m_p n_{\text{H,equiv}} R_b^4} \right)^{1/2} = 3.59 E_{52}^{1/2} t_d^{1/2} n_{\text{H,equiv}}^{-1/2} R_{b,17}^{-2}. \quad (55)$$

Here $E_{52} \equiv (E/10^{52} \text{ ergs})$, t_d is the observed time in units of days, and $R_{b,17} \equiv (R_b/10^{17} \text{ cm})$ (see eq. [5]). The expression for the flux correction factor remains the same as in the weakly-cooling-PWB case; the displayed plots indicate, however, that $F_{\nu,\text{max}}$ undergoes large variations across the bubble when the particle-conservation constraint is imposed (although not when the terminal speed is fixed). Although the factor A_{correct} alters the parameter dependences of the break frequencies (specifically, $\nu_m \propto Et^{-1} n_{\text{H,equiv}}^{-1/2}$ and $\nu_c \propto E^{-1} t^{-1} n_{\text{H,equiv}}^{-1/2}$ for an adiabatic shock in a strongly cooling bubble), its numerical value will not be large for typical afterglow parameters. This seems to suggest that the standard expressions should provide adequate estimates of the source parameters in this case, too, but we caution that the adopted approximation of an effectively uniform ambient medium becomes questionable at large values of a_1 .²⁶

²⁵In a more precise treatment, one obtains t for radiation emitted along the line of sight to the center from the differential equation $c dt/dr = 1/2\Gamma_{\text{sh}}^2$, where Γ_{sh} is the Lorentz factor of the shock (see Sari 1997). The solution in this case is $t = x/4\Gamma_{\text{sh}}^2 c + R_s/2\Gamma_0^2 c$ (where Γ_0 is the initial Lorentz factor of the outflow and $\Gamma_{\text{sh}}^2 \approx [(1 + \beta_2)/(1 - \beta_2)]\Gamma$ for $\Gamma_{\text{sh}} \gg 1$), which shows that the approximation used in the text is only valid for $x \gg (\Gamma/\Gamma_0)^2 R_s$.

²⁶In the conventional interpretation, the forward shock is expected to be fast-cooling (and, if ϵ_e is close to 1, also radiative) during the early phase of the afterglow evolution. However, in the case of a PWB environment characterized by $\sigma_w \lesssim 1$, the shock can be only partially radiative since a significant fraction of

The above considerations suggest that, as a rough check of the compatibility of the PWB model with observations, one can examine the consistency of the predicted values of $\epsilon_{e,\text{equiv}}$, $\epsilon_{B,\text{equiv}}$, and $n_{\text{H},\text{equiv}}$ with the values of ϵ_e , ϵ_B , and n_{H} that are inferred from the spectral data by using the standard ISM model. The results shown in Figure 4 indicate that, if σ_w is not $\ll 1$, then $\epsilon_{e,\text{equiv}}$ typically lies in the range $\sim 0.1 - 1$. As we noted in §1, such comparatively large values have been inferred for the corresponding standard parameter ϵ_e even before a large body of data became available, based on emission-efficiency considerations as well as on some early model fits. These inferences have been supported by more recent analyses of the accumulating data on afterglows, which have even led to the suggestion that ϵ_e may have a “universal” value ~ 0.3 (Freedman & Waxman 2001; see also Huang, Dai, & Lu 2000 and Panaitescu & Kumar 2002). The predicted magnitudes of $\epsilon_{e,\text{equiv}}$ are larger for smaller values of σ_w and when the fixed- $\beta(R_b)$ constraint is imposed (see Fig. 5). However, these estimates could be lowered in real sources by the admixture of baryons into the bubble interior — either by injection at the source or by evaporation from the bounding supranova-ejecta shell (see footnote 16). Turning next to the magnetic energy-density parameter $\epsilon_{B,\text{equiv}}$, we see from Figures 4 and 5 that values in the range $\lesssim 1$ to $\lesssim 10^{-2}$ are predicted by our model as σ_w decreases from 1 to 10^{-3} . It is noteworthy that this range is consistent with the values inferred in the standard ISM picture for a source like GRB 970508 (which, as we discussed in §1, have posed a challenge for the conventional scenario) as well as with the mean values of ϵ_B inferred for the afterglow sample of Panaitescu & Kumar (2001). In this case one can again expect a reduction in the estimated parameter value as a result of the admixture of baryons (which would reduce the cooling and the associated magnetic field compression in the bubble; see GK), although other factors may also contribute to a lowering of ϵ_B : for example, the afterglow-emitting shock may not be transverse, and the electromagnetic-to-thermal pressure ratio in the diffusive regions of the PWB might be lower than the equipartition value adopted in our model.

Finally, our derived values of $n_{\text{H},\text{equiv}}$ are compatible with the observationally inferred preshock particle densities. The values of n_{H} estimated in the literature under the assumption of a uniform, “cold” ambient medium typically span the range $\sim 0.1 - 50 \text{ cm}^{-3}$ (e.g., Panaitescu & Kumar 2002), although (as noted in the last-cited reference) there are examples of sources where a density $< 10^{-2} \text{ cm}^{-3}$ is implied. There have also been

the shock kinetic energy is converted into postshock magnetic energy, which is not subject to radiative losses. Although one can in principle derive the appropriate expressions also for this situation [as was done, e.g., by Böttcher & Dermer (2000) in the standard case], we do not consider fast-cooling shocks here since the results for partially radiative shocks are more cumbersome and would unduly complicate the presentation.

suggestions in the literature that some afterglows originated in a medium with a density $> 10^2 \text{ cm}^{-3}$. As is seen from Figures 4 and 5, our model can in principle account for all of the inferred values: the typical densities are reproduced by PWBs with τ_{sd} in the range $\sim 3 - 30$, whereas “outlying” low and high inferred densities correspond to lower (respectively, higher) values of the cooling parameter a_1 . The basic trend is for bubbles with more radiative cooling to be characterized by higher values of the equivalent density:²⁷ this follows directly from our adopted parameterization (see §2.1), which implies $n_{\text{H,equiv}} \propto p_1 \propto \tau_{\text{sd}}^{-3} \propto a_1^{3/2}$. It is, furthermore, seen that the effective-density predictions are remarkably insensitive to the choice of the wind magnetization parameter σ_w and of the specific constraint imposed on the solution. This robustness can be traced to the fact that $n_{\text{H,equiv}}$ basically measures the energy density in the bubble, which, for a given choice of a_1 (and thus of $R_b \propto a_1^{-1/2}$), is essentially determined by the wind ram pressure at a distance $\sim R_b$ from the center.

Another attractive feature of the PWB scenario is that it naturally gives rise to radial profiles of $n_{\text{H,equiv}}$ that, depending on the cooling parameter a_1 and the location within the bubble (see the plots of $2 - k$ in Figs. 4 and 5), may resemble a uniform medium (constant- n_{H} ISM or interstellar cloud) or a stellar wind ($n_{\text{H}} \propto r^{-2}$; but note that k strictly remains $\gtrsim 1$ in these solutions). Both types of behavior have, in fact, been inferred in afterglow sources (e.g., Chevalier & Li 2000; Frail et al. 2000; Halpern et al. 2000). The unique aspect of the radial distribution of $n_{\text{H,equiv}}$ in this picture is that it spans a range of effective power-law indices k that can vary from source to source, and, moreover, that the value of k appropriate to any given afterglow is predicted to change with time as the afterglow-emitting shock propagates within the bubble. This leads to a more flexible modeling framework for the afterglow evolution and can naturally accommodate cases where a value of k that is intermediate between those of a uniform ISM and a stellar wind could best fit the observations (see, e.g., Livio & Waxman 2000). It also explains why afterglows associated with star-forming regions need not show evidence of a stellar-wind environment (as expected when the GRB progenitor is a massive star; in view of the derived magnitudes of $n_{\text{H,equiv}}$, this model also makes it possible to understand how a source with such a progenitor could produce an afterglow with an implied value of n_{H} that was much lower than the typical ambient density near massive stars). In addition, high values of $n_{\text{H,equiv}}$ in this picture are not subject to the objection (e.g., Halpern et al. 2000) that

²⁷In particular, afterglows with inferred preshock densities above $\sim 10 \text{ cm}^{-3}$ are expected in this picture to arise in highly radiative PWBs, suggesting that such sources may be the most promising candidates for testing the predicted departures from the standard spectral scaling relations (which, according to our preceding arguments, should be most pronounced in rapidly cooling bubbles).

they will necessarily give rise to excess extinction (although it is also conceivable that dust destruction by the optical-UV and X-ray radiation from the GRB outflow could reduce any preexisting extinction toward the source; see Waxman & Draine 2000 and Fruchter, Krolik, & Rhoads 2001). As is seen from Figures 4 and 5, the predicted $n_{\text{H,equiv}}(r)$ distributions exhibit progressively steeper declines as the outer boundary of the bubble is approached. This suggests that the later phases of the evolution of any given afterglow would be more likely to exhibit signatures of a stellar-wind environment. In all the $\sigma_w \geq 0.1$ bubbles, this wind-like behavior becomes more pronounced the lower the value of the cooling parameter a_1 . Since (as noted above) the value of $n_{\text{H,equiv}}$ also exhibits a systematic dependence on this parameter (it decreases with decreasing a_1), one may expect afterglows with higher inferred ambient densities to preferentially indicate a uniform ISM-like environment if they originate in such bubbles.

The inferred radii of afterglow shocks typically lie between $\gtrsim 10^{17}$ cm and $\lesssim 10^{18}$ cm (e.g., Piran 1999; Chevalier & Li 2000). These values are consistent with the upper limit on the bubble’s outer radius (eq. [5]) for supranova–GRB time delays of $\gtrsim 1$ yr to $\lesssim 10$ yr. We can check on whether typical afterglow-emitting shocks will still be relativistic by the time they reach the outer edge of the bubble at R_b by solving the adiabatic evolution equation

$$[\Gamma^2(r) - 1]M_{\text{eq}}(r) + [\Gamma(r) - 1]M_0 = (\Gamma_0 - 1)M_0, \quad R_s < r < R_b \quad (56)$$

where

$$M_{\text{eq}}(r) \equiv \int_{R_s}^r 4\pi R^2 n_{\text{H,equiv}}(R) m_p dR \quad (57)$$

and $M_0 \equiv E/\Gamma_0 c^2$ (e.g., van Paradijs et al. 2000). The bottom panels in Figures 4 and 5 show the results for the PWB solutions presented in §2.3 using a representative value of Γ_0 and two plausible values of E . It is seen that, in all cases, the GRB outflow decelerates rapidly after entering the bubble, and in weakly cooling PWBs the Lorentz factor of the afterglow-emitting gas is at most a few by the time the shock reaches R_b (and is effectively nonrelativistic for the $E = 10^{52}$ ergs solutions). Only in the case of an energetic shock and a strongly cooling bubble is $\Gamma(R_b)$ appreciable (but even then it remains $\lesssim 10$). It is worth bearing in mind, however, that, if the outflow is collimated with a small opening half-angle θ_j , then it will start to strongly decelerate due to lateral spreading when its Lorentz factor decreases to $\sim 1/\theta_j$ (e.g., Sari, Piran, & Halpern 1999; Rhoads 1999), so that even the more energetic shocks could become nonrelativistic while they are still inside the PWB.²⁸ These results are again quite insensitive to the value of σ_w and to the choice of the imposed

²⁸Mass loading of the bubble by evaporation of the ejecta shell will further contribute to the lowering of Γ .

constraint; this is not surprising in view of the fact that they depend mostly on the behavior of $n_{\text{H,equiv}}(\tilde{r})$, which exhibits a similar trend.

A GRB shock that reaches the supranova ejecta shell at $r = R_b$ with a Lorentz factor > 1 would be rapidly decelerated to subrelativistic speeds since the rest-mass energy of the shell ($\sim 2 \times 10^{55} M_{\text{ej},10}$ ergs, where $M_{\text{ej},10} \equiv M_{\text{ej}}/10 M_{\odot}$) is in most cases much greater than the (equivalent isotropic) shock energy E . The spectral characteristics of the forward shock after it enters the shell could be evaluated once the dynamical evolution of the shock is calculated.²⁹ Besides the anticipated alterations in the spectral scaling laws, one may expect the numerical values of the various physical parameters to undergo dramatic changes as the shock moves from the interior of the bubble to the ejecta shell: in particular, n_{H} would likely increase by several orders of magnitude, whereas ϵ_e and ϵ_B would probably decrease significantly. In addition, the sudden deceleration would drive a relativistic reverse shock into the GRB outflow, whose emission may have an important effect. The overall outcome is likely to be a discontinuous change in the shape and evolution of the observed spectrum. Ramirez-Ruiz et al. (2001) modeled a somewhat similar situation that may arise when a GRB shock that propagates in a stellar wind encounters a density bump. They suggested that an encounter of this type could induce a brightening and reddening of the afterglow spectrum and might explain observations of such a behavior in several sources. The situation considered by Ramirez-Ruiz et al. (2001) differs, however, from a PWB–SNR transition in that the density contrast as well as the jumps in ϵ_e and ϵ_B (which were assumed to be negligible in the “bump in a wind” model) would typically be much larger in the latter case. It would thus be interesting to carry out a detailed investigation of the observational implications of the shock encounter with a dense shell in the explicit context of the PWB model.

3.2. Interpretation of X-Ray Features in the Supranova/PWB Model

The SNR shell bounding the PWB could also manifest itself by imprinting X-ray features on the GRB afterglow spectrum. Indeed, recent detections of such features in several GRB sources have been argued to provide strong support for the supranova scenario (e.g., Lazzati, Campana, & Ghisellini 1999; Piro et al. 2000; Vietri et al. 2001; Amati et al. 2000; Lazzati et al. 2001; Böttcher, Fryer, & Dermer 2002). To date, four GRB

²⁹Although the behavior of the shock in both the highly relativistic and the Newtonian limits had been considered in the literature, so far there has been no published treatment of the transition between these two regimes.

sources (GRB 970508, GRB 970828, GRB 991216, GRB 000214), observed $\sim 8 - 40$ hr after the burst, showed emission features in their postburst X-ray spectrum, and one source (GRB 990705) exhibited an absorption feature that disappeared 13 s after the onset of the burst. These features most likely represent Fe $K\alpha$ lines or an iron K edge, and their detection implies that a large quantity ($\gtrsim 0.1 M_{\odot}$) of pure iron is located in the vicinity ($r \lesssim 10^{16}$ cm) of the GRB source. Such a large iron mass is most naturally produced in a supernova explosion, and the inferred distance of the absorber indicates that the supernova event preceded the GRB by at least several months, as expected in the supranova picture. The association with a supranova is further strengthened by the argument (Vietri et al. 2001) that the abundance of ^{56}Fe (the product of the radioactive decay of ^{56}Ni and ^{56}Co) in supernova ejecta is not expected to become significant until $\sim 10^2$ days after the explosion, during which time the ejected gas in a source like GRB 991216 (in which the observed line width is consistent with an outflow speed $\sim 0.1 c$; Piro et al. 2000) would have traveled to a distance $\gtrsim 10^{16}$ cm from the origin.

We now proceed to discuss how the observed X-ray features can be interpreted in the context of the supranova scenario, and we consider the implications of this interpretation to the PWB afterglow model presented in this paper. We concentrate on the specific example of GRB 991216, which allows us to capitalize on the analysis already carried out on this object by Piro et al. (2000) and Vietri et al. (2001); our interpretation does, however, differ in its details from the model favored by the latter authors. We approximate the ejecta as a thin spherical shell of radius R_{ej} and density n_{ej} . Although the ejecta of a supernova that is not associated with a pulsar may be expected to fill the volume into which it expands, in the case of an inflating PWB the ejecta will be swept up and compressed into a dense shell (e.g., Chevalier 1977). The acceleration of this shell by the lower-density bubble gas would subject it to a Rayleigh-Taylor instability, which could lead to clumping (see, e.g., Jun 1998). As we argue below, such clumping is consistent with the data for GRB 991216.³⁰

We assume that the emission is induced by continuum irradiation from the central region that commences around the time of the burst but is not necessarily confined to the solid angle of the GRB outflow. The part of the shell that is observable to us at time t is limited by light-travel effects, so that, for a source observed up to time t_{max} , the solid angle $\Delta\Omega$ from which Fe emission is received is given by

$$\frac{\Delta\Omega}{4\pi} = \frac{1 - \cos\theta_{\text{max}}}{2} = \frac{ct_{\text{max}}}{2(1+z)R_{\text{ej}}} = \frac{1.1 \times 10^{15} \text{ cm}}{R_{\text{ej}}}, \quad (58)$$

³⁰The presence of a strongly clumped shell was already inferred by Lazzati et al. (2000) in GRB 990705 from their analysis of the X-ray absorption feature in that source.

where the angle θ is measured with respect to the line of sight to the origin, and where we substituted numerical values appropriate to GRB 991216 (redshift $z = 1.02$, $t_{\max} = 40.4$ hr). Piro et al. (2000) identified the X-ray feature in GRB 991216 as an Fe XXVI H α line (rest energy 6.97 keV) with a FWHM (as quoted in Lazzati et al. 2001) of $\sim 0.15c$. Since we attribute the emission to material that moves toward the observer with a speed of that order, we favor an identification with a lower-energy line, specifically Fe XXV He α (rest energy 6.7 keV), but our results are not sensitive to this choice.³¹ Based on the photoionization models of Kallman & McCray (1982), Fe XXV is the dominant ion when the ionization parameter $\xi \equiv L_i/n_{\text{ej}}R_{\text{ej}}^2$ (where L_i is the ionizing continuum luminosity) lies in the range $\log \xi \sim 2.7 - 3.2$. Using $L_i = 4\pi D^2 F_x \equiv L_{i,45} 10^{45}$ ergs s $^{-1}$, with $F_x = 2.3 \times 10^{-12}$ ergs cm $^{-2}$ s $^{-1}$ and $D = 4.7$ Gpc (Piro et al. 2000), we thus infer

$$n_{\text{ej}}R_{\text{ej}}^2 = 6.1 \times 10^{42} (L_{i,45}/6.1) (\xi/10^3)^{-1}. \quad (59)$$

The observed line luminosity corresponds to $\dot{N}_{\text{Fe},52} \equiv (\dot{N}_{\text{Fe}}/10^{52} \text{ photons s}^{-1}) = 8$ (Piro et al. 2000), and we can write $\dot{N}_{\text{Fe}} = (\Delta\Omega/4\pi)M_{\text{Fe}}/56m_p t_{\text{rec}}$, where $M_{\text{Fe}} = 0.1M_{\text{Fe},0.1} M_{\odot}$ is the total iron mass in the shell and $t_{\text{rec}} \approx 4 \times 10^9 T_6^{0.6} Z^{-2} n_e^{-1} = 2.8 \times 10^{10} T_6^{0.6} n_e^{-1}$ s is the recombination time for a $Z = 24$ ion (with T_e and n_e being the electron temperature and number density, respectively, and Z the ion charge). The expression for t_{rec} is valid in the range $T_e \sim 10^2 - 10^6$ K (Lazzati et al. 2001), and photoionization models imply that $T_6 \equiv T_e/10^6$ K ≈ 1 for $\log \xi \approx 3$ (Kallman & McCray 1982). Approximating $n_e \approx n_{\text{ej}}$, we obtain

$$n_{\text{ej}} = 1.0 \times 10^9 (4\pi/\Delta\Omega) T_6^{0.6} (\dot{N}_{\text{Fe},52}/8) M_{\text{Fe},0.1}^{-1} \text{ cm}^{-3}. \quad (60)$$

Substituting equation (60) into equation (59) gives

$$R_{\text{ej}} = 7.6 \times 10^{16} (\Delta\Omega/4\pi)^{0.5} M_{\text{Fe},0.1}^{0.5} (\dot{N}_{\text{Fe},52}/8)^{-0.5} (L_{i,45}/6.1)^{0.5} T_6^{-0.3} (\xi/10^3)^{-0.5} \text{ cm}. \quad (61)$$

Combining equations (61) and (58) then yields

$$R_{\text{ej}} = 1.9 \times 10^{16} M_{\text{Fe},0.1}^{1/3} (\dot{N}_{\text{Fe},52}/8)^{-1/3} (L_{i,45}/6.1)^{1/3} T_6^{-1/5} (\xi/10^3)^{-1/3} \text{ cm} \quad (62)$$

and (for the given fiducial values) $\theta_{\max} \approx 28^\circ$. Substituting the estimate (62) into the relation (59) in turn implies

$$n_{\text{ej}} = 1.8 \times 10^{10} M_{\text{Fe},0.1}^{-2/3} (\dot{N}_{\text{Fe},52}/8)^{2/3} (L_{i,45}/6.1)^{1/3} T_6^{2/5} (\xi/10^3)^{-1/3} \text{ cm}^{-3}. \quad (63)$$

³¹An independent argument for an identification of the X-ray feature in a source like GRB 991216 with the Fe XXV He α line was presented by Ballantyne & Ramirez-Ruiz (2001), who demonstrated that an Fe XXVI H α line is unlikely to be observed because of the removal of photons from the line core by Compton scattering.

If the shell expands with a speed $v_{\text{ej}} \approx 0.1c$ (see §2.1), then its age when it reaches the radius given by equation (62) is

$$t_{\text{age}} \approx 72 M_{\text{Fe},0.1}^{1/3} (\dot{N}_{\text{Fe},52}/8)^{-1/3} (L_{i,45}/6.1)^{1/3} T_6^{-1/5} (\xi/10^3)^{-1/3} (v_{\text{ej}}/0.1c)^{-1} \text{ days} . \quad (64)$$

This value is consistent with the time required for the bulk of the ejected radioactive ^{56}Ni to decay into ^{56}Fe .

The electron column density in the X-ray emitting portion of the shell is given by $N_e = M_{\text{ej}}/4\pi R_{\text{ej}}^2 f_A \mu_e m_p$, where f_A is the covering factor of the shell and μ_e , the electron molecular weight, is 2 for hydrogen-free ejecta. Assuming $f_A \approx 1$ and using the estimate (62), the Thomson optical depth of the shell is inferred to be

$$\tau_{\text{T}} = 0.9 M_{\text{ej},10} M_{\text{Fe},0.1}^{-2/3} (\dot{N}_{\text{Fe},52}/8)^{2/3} (L_{i,45}/6.1)^{-2/3} T_6^{2/5} (\xi/10^3)^{2/3} (\mu_e/2)^{-1} . \quad (65)$$

For these fiducial values, the thickness of a homogeneous shell would be $\sim 8 \times 10^{13}$ cm, which is consistently $\ll R_{\text{ej}}$. It is, however, more likely that this nominal thickness corresponds to the size of a clump in a shell with a small volume filling factor (see Lazzati et al. 2001). In fact, a high degree of clumping is also indicated by the requirement that the line photons reach the observer without undergoing excessive Compton broadening in the shell. The photoionization optical depth of the iron ions in the shell is similarly inferred to be

$$\tau_{\text{Fe}} = 4.4 M_{\text{Fe},0.1}^{1/3} (\dot{N}_{\text{Fe},52}/8)^{2/3} (L_{i,45}/6.1)^{-2/3} T_6^{2/5} (\xi/10^3)^{2/3} (\eta/0.5) , \quad (66)$$

where η is the relative abundance of the Fe XXV ion (e.g., Kallman & McCray 1982) and where we used $\sigma_{\text{FeXXV}} \approx 2.0 \times 10^{-20}$ cm $^{-2}$ (e.g., Krolik & Kallman 1987). (Our fiducial mass ratio $M_{\text{Fe}}/M_{\text{ej}} = 0.01$ corresponds to an iron abundance that is ~ 5.6 times the solar value.) The estimated values of $\tau_{\text{T}} (\lesssim 1)$ and τ_{Fe} (a few) are optimal for producing high-equivalent-width iron lines through reflection (e.g., Weth et al. 2000; Vietri et al. 2001). Since, in this picture, $\tau_{\text{Fe}} \propto 1/R_{\text{ej}}^2$, the efficiency of producing detectable emission lines would typically be low for shells with radii much in excess of $\sim 10^{16}$ cm (eq. [62]).

The most natural way of relating the above scenario to the PWB model is to identify t_{age} with t_{sd} and R_{ej} with R_b . However, such a straightforward identification is problematic in that the magnitude of R_{ej} that is inferred from the X-ray emission-line observations ($\lesssim 10^{16}$ cm; eq. [61]) is at least an order of magnitude smaller than the lower limit on R_b typically implied by the afterglow data. In particular, in the case of GRB 991216, the optical light curve showed evidence for steepening (which was attributed to shock deceleration triggered by the lateral spreading of a jet) starting about 2 days after the burst (Halpern et al. 2000). For this time scale to be consistent with an emission radius $\sim 10^{16}$ cm, the relation $t \lesssim (1+z)r/4c\Gamma^2$ implies that the flow Lorentz factor must be $\lesssim 2$.

However, given the comparatively high ($\sim 10^{53} - 10^{54}$ ergs) equivalent isotropic energy inferred for the emitting shock, it is unlikely that the Lorentz factor could become so low over such a relatively short distance (see bottom panels in Figs. 4 and 5). The problem is even more acute for GRB 970508, in which the X-ray emission feature detected ~ 1 day after the burst again implies an emission radius $\sim 10^{16}$ cm (e.g., Lazzati et al. 1999), but where model fitting of the afterglow spectrum ~ 1 week after the GRB yields a radial scale $\gtrsim 3 \times 10^{17}$ cm along the line of sight to the center [see references in §1; this result is supported by radio scintillation measurements (Frail et al. 1997)]. These values are mutually inconsistent, since the SNR shell could not have reached a distance of $\gtrsim 0.1$ pc in one week even if it expanded at the speed of light. As we noted in §3.1, the afterglow emitting gas should decelerate rapidly after the forward shock encounters the SNR shell, and the shock transition into the shell would likely result in a discontinuous variation in the afterglow light curve. If the radius of the shell indeed corresponds to the value of R_{ej} indicated by the X-ray emission-line data, then this is hard to reconcile with the fact that, in the case of GRB 970508, the light curve remained detectable and more or less smooth during a 450-day monitoring period, with the underlying flow evidently becoming nonrelativistic only after ~ 100 days (Frail, Waxman, & Kulkarni 2000; see also Chevalier & Li 2000).

The discrepancy between the inferred radius of the X-ray line-emitting shell and the deduced radial distance of the afterglow-emitting shock may be reconciled within the framework of the supranova/PWB scenario if the SNR shell and the PWB are not spherically symmetric. One possibility (suggested by Lazzati et al. 1999 and Vietri et al. 2001) is that the supernova explosion does not eject matter along the SMNS rotation axis, where the GRB outflow is subsequently concentrated. An alternative possibility (which we discuss below) is that both the SNR and the PWB become elongated in the polar directions because of a preexisting density anisotropy in the GRB environment. Under these circumstances, a highly collimated GRB outflow (such as the one inferred in GRB 991216; Halpern et al. 2000) could reach a distance $\gtrsim 10^{17}$ cm without encountering the SNR shell even as the lower-latitude regions of the shell (from which the X-ray line emission emanates) have radii $\lesssim 10^{16}$ cm. In the case of GRB 991216, where the X-ray observations lasted between 37 and 40.4 hr after the burst (Piro et al. 2000), the inferred effective spherical radius of the X-ray emitting shell (eq. [61]) strictly corresponds only to angles θ that lie in the narrow range $\sim 27 - 28^\circ$ (see eq. [58]). If the jet opening half-angle is significantly smaller than these values and R_b is $\gg 10^{16}$ cm at small values of θ , then the afterglow observations can in principle be consistent with the X-ray emission-line measurements.³²

³²The detection of an X-ray absorption feature would be compatible with this interpretation if it could be

The formation of a highly elongated PWB in the supranova scenario may be a natural outcome of the manner in which its environment was shaped by the progenitor star as well as of its intrinsic physical properties. The star that gave rise to an SMNS in a supranova event must have been massive, rapidly rotating, and magnetized. It would have influenced the density distribution in its vicinity through episodes of strong mass loss, in particular during its red-supergiant and blue-supergiant evolutionary phases. There is strong observational evidence that the “slow” red-supergiant wind is often anisotropic (possibly as a result of fast-rotation and magnetic effects), transporting significantly more mass near the equatorial plane than in the polar regions. Subsequent stellar outflows that propagate into this mass distribution will assume an elongated morphology: this has been the basis of the “interacting stellar winds” class of models for the shapes of planetary nebulae (e.g., Dwarkadas, Chevalier, & Blondin 1996), in which the outflow represents the “fast” blue-supergiant wind, as well as of models of apparent SNR “protrusions,” in which the outflow corresponds to the supernova ejecta (e.g., Blondin, Lundqvist, & Chevalier 1996). In these applications, the subsequent outflows have been taken to be effectively spherically symmetric. However, an even stronger collimation is achieved if the later outflow is itself anisotropic. In particular, if the fast wind is even weakly magnetized (with a dominant azimuthal field component), then, after passing through the wind shock where the field is amplified (an effect that will be especially strong if cooling is important behind the shock), the magnetic hoop stress will collimate the resulting interstellar bubble (e.g., Chevalier & Luo 1994). In fact, as was argued by Gardiner & Frank (2001), the collimation may start even before the shock is encountered; this should be particularly pronounced in cases where magnetic stresses also play a dominant role in driving the fast wind (as in the Wolf-Rayet wind model of Biermann & Cassinelli 1993). The additional collimation provided by the magnetic field was suggested as the origin of strongly elongated planetary nebulae, which cannot be readily explained by purely hydrodynamic models.

A pulsar wind expanding into the anisotropic density distribution created by the earlier (red-supergiant and blue-supergiant) stellar outflows will give rise to an elongated bubble (see, e.g., Li & Begelman 1992 for a discussion of PWB evolution in a stratified medium). Furthermore, since the pulsar wind is highly magnetized and cooling may be important in the supranova-induced PWB (see §2.3), the same magnetic collimation effects that are invoked in the modeling of planetary nebulae will act to increase the bubble elongation in

demonstrated that the absorbing material was also located at a distance $\gg 10^{16}$ cm from the irradiating-continuum source. In the only such case reported to date (GRB 990705), Lazzati et al. (2001) deduced a radius $\sim 10^{16}$ cm using a similar scheme to the one applied here to the interpretation of X-ray line emission. They have, however, also argued that the afterglow emission properties in this object may be consistent with a shock/SNR-shell encounter on this radial scale.

this case too. [In fact, the collimating effect of magnetic hoop stresses on plerionic supernova remnants was already discussed by Rees & Gunn (1974); it was subsequently modeled by Begelman & Li (1992).] Under these combined effects, it is quite plausible to expect that a bubble aspect ratio $\gtrsim 10$ could be achieved, although this needs to be confirmed by an explicit calculation.³³ Previous numerical simulations of outflows expanding into an anisotropic medium also make it likely that the column density of the swept-up SNR shell will be lower near the apex of the bubble than at larger values of θ , which should be relevant to the modeling of X-ray absorption and emission features as well as of the afterglow light curve. The expected departure of the PWB from sphericity might require a modification of the model presented in §2.2, which would probably be best done with guidance from numerical simulations. We nevertheless anticipate that the results obtained from the semianalytic model would remain at least qualitatively valid. Furthermore, if a strong elongation only occurs near the symmetry axis (which would be consistent with the data for GRB 991216 as well as with some of the existing numerical simulations), then even the quantitative predictions of the simple spherical model would still be approximately correct.

4. Conclusions

We propose to identify the environment into which afterglow-emitting shocks in at least some GRB sources propagate with pulsar-wind bubbles. Our results can be summarized as follows:

- PWBs provide a natural resolution of the apparent difficulty of accounting for the high electron and magnetic energy fractions (ϵ_e and ϵ_B , respectively) inferred in a number of afterglow sources. This is because pulsar winds are expected to have a significant e^\pm component and to be highly magnetized. If high values of ϵ_e in fact prove to occur commonly in afterglow sources, then this would strengthen the case for a simple, “universal” explanation of this type.
- An association of PWBs with GRBs is expected under several GRB formation scenarios, including the collapse of a massive star. In light of suggestive evidence that many of the afterglows observed to date may have a massive stellar progenitor, we

³³In this case the width and centroid redshift of the observed X-ray emission lines may not be due entirely to the bulk motion of the SNR shell but may also have significant contributions from Compton broadening within the shell; see Vietri et al. 2001.

have concentrated on this case. In particular, we considered the supranova scenario of VS, in which an intense pulsar-type wind from the GRB progenitor is a key ingredient of the hypothesized evolution. In this picture, the ejection of a highly energetic, ultrarelativistic pulsar wind is predicted to follow the supernova explosion and to last anywhere from several months to several years until the central object collapses to form a black hole, thereby triggering the burst. Recent detections of X-ray features in several GRB sources have been interpreted as providing strong support for this scenario.

- To assess the implications of a PWB environment to afterglow sources in the context of the supranova scenario, we have constructed a simple, steady-state model of the early-time structure of a plerionic supernova remnant. We have been guided by Atoyan’s (1999) spectral modeling of the Crab, which yielded a lower initial wind Lorentz factor and a higher initial pulsar rotation rate than in previous estimates, and by other recent results on the Crab and Vela synchrotron nebulae, from which we inferred a plausible range of the wind magnetization parameter σ_w ($\sim 10^{-3} - 1$). In contradistinction to previous models of the structure of plerionic SNRs, we have replaced the assumption that ideal MHD applies throughout the PWB with the postulate that the electromagnetic-to-thermal pressure ratio in the bubble remains constant after it increases to ~ 1 . We have also explicitly incorporated synchrotron-radiation cooling. Although our solutions do not provide an exact representation of radiative (and thus intrinsically time-dependent) PWBs, we have verified that they generally do not depend on the detailed approximations that are adopted and are essentially characterized by σ_w and by a second parameter that measures the relative importance of radiative cooling within the bubble. It would be of interest to further develop this model and to investigate the possibility that it can be applied both to young radio pulsars and to GRB progenitors as members of the same general class of rapidly rotating and strongly magnetized neutron stars.
- In view of the “hot” (relativistic) equation of state and high magnetization of the shocked wind, the effective hydrogen number density that determines the properties of a relativistic afterglow-emitting shock is given by $n_{\text{H,equiv}} = [4p + (B' + \mathcal{E}')^2/4\pi]/m_p c^2$, where B' and \mathcal{E}' are, respectively, the comoving magnetic and electric fields and p is the particle pressure. For plausible values of the cooling parameter (and independent of the value of σ_w), the derived values of $n_{\text{H,equiv}}$ span the density range inferred from spectral modeling of GRB afterglows. An interesting feature of the solutions is the predicted radial variation of $n_{\text{H,equiv}}$ within the bubble, which can mimic either a uniform-ISM or a stellar-wind environment, but which in general exhibits a more diverse behavior. Among other things, this model makes it possible to understand how

a GRB with a massive progenitor can produce an afterglow that shows no evidence of a stellar-wind or a high-density environment.

- We have examined the dependence of the characteristic synchrotron spectral quantities in an afterglow-emitting shock that propagates inside a PWB on the bubble parameters and related them to the standard expressions derived under the assumption of a uniform-ISM environment. We found that, under typical circumstances, the standard expressions remain roughly applicable if one substitutes for ϵ_e , ϵ_B , and n_H their “equivalent” PWB expressions. We noted, however, that the parameter scaling laws would change in strongly radiative bubbles: these differences might be detectable in objects with high inferred ambient densities.
- Finally, we considered the possible observational manifestations of the dense supranova shell that surrounds the PWB in this picture. In particular, we discussed how the X-ray emission features detected in objects like GRB 991216 may be interpreted in the context of a supranova-generated PWB. We concluded that both the X-ray features and the afterglow emission could be explained by this model if the PWB were elongated, and we argued that such a shape might be brought about by anisotropic mass outflows from the GRB progenitor star.

We are grateful to N. Vlahakis for pointing out to us the need to account for the comoving electric field in the PWB structure equations, and to the anonymous referee for encouraging us to broaden the parameter range covered by our solutions. We also thank J. Arons, J. Blondin, A. Frank, A. Heger, D. Lamb, C. Litwin, A. Olinto, T. Piran, E. Ramirez-Ruiz, M. Rees, M. Vietri, and S. Woosley for useful conversations or correspondence. AK acknowledges a Forchheimer Fellowship at the Hebrew University, where this work was begun. JG acknowledges a Priscilla and Steven Kersten Fellowship at the University of Chicago. This research was supported in part by NASA grant NAG 5-9063 (AK) and by NSF grant PHY-0070928 (JG).

REFERENCES

- Amati, L., et al. 2000, *Science*, 290, 953
- Andersson, N. 1998, *ApJ*, 502, 708
- Arons, J. 1998, *MmSAI*, 69, 989

- Arons, J. 2002, in *Neutron Stars in Supernova Remnants*, ed. P.O. Slane & B. M. Gaensler (San Francisco: ASP), in press (astro-ph/0201439)
- Atoyan, A. M. 1999, *A&A*, 346, L49
- Ballantyne, D. R., & Ramirez-Ruiz, E. 2001, *ApJ*, 559, L83
- Begelman, M. C. 1998, *ApJ*, 493, 291
- Begelman, M. C., & Li, Z.-Y. 1992, *ApJ*, 397, 187
- Bhattacharya, D., & Srinivasan, G. 1995, in *X-Ray Binaries*, ed. W. H. G. Lewin, J. van Paradijs, & E. P. J. van den Heuvel (Cambridge: Cambridge University Press), 495
- Biermann, P. I., & Cassinelli, J. P. 1993, *A&A*, 277, 691
- Blackman, E. G., & Yi, I. 1998, *ApJ*, 498, L31
- Blandford, R. D. 2000, in *Cosmic Explosions*, Proc. 10th Maryland Conf. on Astrophysics, ed. S. S. Holt & W. W. Zhang (New York: AIP), 23
- Blasi, P., Epstein, R. I., & Olinto, A. 2000, *ApJ*, 533, L123
- Blondin, J. M., Lundqvist, P., & Chevalier, R. A. 1996, *ApJ*, 472, 257
- Bocquet, M., Bonazzola, S., Gourgoulhon, E., & Novak, J. 1995, *A&A*, 301, 757
- Böttcher, M., & Dermer, C. D. 2000, *ApJ*, 532, 281
- Böttcher, M., & Fryer, C. L. 2001, *ApJ*, 547, 338
- Böttcher, M., Fryer, C. L., & Dermer, C. D. 2002, *ApJ*, 567, 441
- Bykov, A. M., & Mészáros, P. 1996, *ApJ*, 461, L37
- Chevalier, R. A. 1977, in *Supernovae*, ed. D. N. Schramm (Dordrecht: Reidel), 53
- Chevalier, R. A. 1998, *MmSAI*, 69, 977
- Chevalier, R. A. 2000, *ApJ*, 539, L45
- Chevalier, R. A., & Li, Z.-Y., 2000, *ApJ*, 536, 195
- Chevalier, R. A., & Luo, D. 1994, *ApJ*, 421, 225
- Chiueh, T., Li, Z.-Y., & Begelman, M. C. 1998, *ApJ*, 505, 835

- Cook, G. B., Shapiro, S. L., & Teukolsky, S. A. 1994, *ApJ*, 424, 823
- Dwarkadas, V. V., Chevalier, R. A., & Blondin, J. M. 1996, *ApJ*, 457, 773
- Emmering, R. T., & Chevalier, R. A. 1987, *ApJ*, 321, 334
- Farrar, G. R., & Piran, T. 2000, preprint (astro-ph/0010370)
- Frail, D. A., et al. 2000, *ApJ*, 534, 559
- Frail, D. A., Kulkarni, S. R., Nicastro, L., Feroci, M., & Taylor, G. B. 1997, *Nature*, 389, 261
- Frail, D. A., Waxman, E., & Kulkarni, S. R. 2000, *ApJ*, 537, 191
- Freedman, D. L., & Waxman, E. 2001, *ApJ*, 547, 922
- Fruchter, A. S., Krolik, J. H., & Rhoads, J. E. 2001, *ApJ*, 563, 597
- Gallant, Y. A., & Achterberg, A. 1999, *MNRAS*, 305, L6
- Gallant, Y. A., & Arons, J. 1994, *ApJ*, 435, 230
- Gardiner, T. A., & Frank, A. 2001, *ApJ*, 557, 250
- Granot, J., & Königl, A. 2001, *ApJ*, 560, 145 (GK)
- Granot, J., Piran, T. & Sari, R. 1999, *ApJ*, 527, 236
- Granot, J., Piran, T. & Sari, R. 2000, *ApJ*, 534, L163
- Grimsrud, O. M., & Wasserman, I. 1998, *MNRAS*, 300, 1158
- Gruzinov, A. 1999, *ApJ*, 525, L29
- Haensel, P., Lasota, J.-P., & Zdzunik, J. L. 1999, *A&A*, 344, 155
- Halpern, J. P., et al. 2000, *ApJ*, 543, 697
- Helfand, D. J., Gotthelf, E. V., & Halpern, J. P. 2001, *ApJ*, 556, 380
- Huang, Y. F., Dai, Z. G., & Lu, T. 2000, *A&A*, 355, L43
- Inoue, S., Guetta, D., & Pacini, F. 2001, *ApJ*, submitted (astro-ph/0111591)
- Jun, B.-I. 1998, *ApJ*, 499, 282

- Kallman, T. R., & McCray, R. 1982, *ApJS*, 50, 263
- Kennel, C. F., & Coroniti, F. V. 1984, *ApJ*, 283, 694
- Kennel, C. F., Gedalin, M. E., & Lominadze, J. G. 1988, in *Proceedings of the Joint Varenna-Abastumani International School and Workshop on Plasma Astrophysics (ESA SP-285)*, Vol. I, 137
- Kirk, J. G., Guthman, A. W., Gallant, Y. A., & Achterberg, A. 2000, *ApJ*, 542, 235
- Kluźniak, W., & Ruderman, M. 1998, *ApJ*, 505, L113
- Königl, A. 1980, *Phys. Fluids*, 23, 1083
- Kumar, P., & Panaitescu, A. 2000, *ApJ*, 541, L9
- Krolik, J. H., & Kallman, T. R. 1987, *ApJ*, 320, L5
- Lai, D., Chernoff, D. F., & Cordes, J. M. 2001, *ApJ*, 549, 1111
- Lazzati, D., Campana, S., & Ghisellini, G. 1999, *MNRAS*, 304, L31
- Lazzati, D., Ghisellini, G., Amati, L., Frontera, F., Vietri, M., & Stella, L. 2001, *ApJ*, 556, 471
- Li, Z.-Y., & Begelman, M. C. 1992, *ApJ*, 400, 186
- Livio, M., & Waxman, E. 2000, *ApJ*, 538, 187
- Lloyd, N. M., & Petrosian, V. 2000, *ApJ*, 543, 722
- Lyutikov, M., & Blackman E. G. 2001, *MNRAS*, 321, 177
- Medvedev, M. V., & Loeb, A. 1999, *ApJ*, 526, 697
- Mészáros, P. 2001, *Science*, 291, 79
- Mészáros, P., & Rees, M. J. 1997, *ApJ*, 482, L29
- Mészáros, P., Ramirez-Ruiz, E., & Rees, M. J. 2001, *ApJ*, 554, 660
- Milgrom, M., & Usov, V. 1995, *ApJ*, 449, L37
- Panaitescu, A., & Kumar, P. 2002, *ApJ*, in press (astro-ph/0109124)
- Panaitescu, A., & Mészáros, P. 1998, *ApJ*, 501, 772

- Piran, T. 1999, *Phys. Rep.*, 314, 575
- Piro, L., et al. 2000, *Science*, 290, 955
- Pohl, M., & Schlickeiser, R. 2000, *A&A*, 354, 395
- Popham, R., Woosley, S. E., & Fryer, C. 1999, *ApJ*, 518, 356
- Ramirez-Ruiz, E., Dray, L. M., Madau, P., & Tout, C. A. 2001, *MNRAS*, 327, 829
- Rees, M. J., & Gunn, J. E. 1974, *MNRAS*, 167, 1
- Reynolds, S. P., & Chevalier, R. A. 1984, *ApJ*, 278, 630
- Rhoads, J. E. 1999, *ApJ*, 525, 737
- Ruderman, M. A., Tao, L., & Kluźniak, W. 2000, *ApJ*, 542, 243
- Ruffert, M., & Janka, H.-Th. 1999, *A&A*, 344, 573
- Salgado, M., Bonazzola, S., Gourgoulhon, E., & Haensel, P. 1994, *A&A*, 291, 155
- Salvati, M., Bandiera, R., Pacini, F., & Woltjer, L. 1998, *MmSAI*, 69, 1023
- Sari, R. 1997, *ApJ*, 489, L37
- Sari, R. & Piran, T. 1999, *ApJ*, 520, 641
- Sari, R., Piran, T., & Halpern, J. P. 1999, *ApJ*, 519, L17
- Sari, R., Piran, T. & Narayan, R. 1998, *ApJ*, 497, L17 (SPN)
- Smolsky, M. V., & Usov, V. V. 2000, *ApJ*, 531, 764
- Spruit, H. C. 1999, *A&A*, 341, L1
- Spruit, H.C., Daigne, F. & Drenkhahn, G. 2001, *A&A*, 369, 694
- Stecker, F. W. 2000, *Astropart. Phys.*, 14, 207
- Thompson, C. 1994, *MNRAS*, 270, 480
- Thompson, C., & Duncan, R. C. 1993, *ApJ*, 408, 194
- Thompson, C., & Madau, P. 2000, *ApJ*, 538, 105
- Usov, V. V. 1994, *MNRAS*, 267, 1035

- van Paradijs, J., Kouveliotou, C., & Wijers, R. A. M. J. 2000, *ARAA*, 38, 379
- van Putten, M. H. P. M., & Ostriker, E. C. 2001, *ApJ*, 552, L21
- Vietri, M. 1995, *ApJ*, 453, 883
- Vietri, M., Ghisellini, G., Lazzati, D., Fiore, F., & Stella, L. 2001, *ApJ*, 550, L43
- Vietri, M., & Stella, L. 1998, *ApJ*, 507, L45 (VS)
- Vietri, M., & Stella, L. 1999, *ApJ*, 527, L43
- Vlahakis, N., & Königl, A. 2001, *ApJ*, 563, L129
- Waxman, E. 1995, *Phys. Rev. Lett.*, 75, 386
- Waxman, E., & Draine, B. T. 2000, *ApJ*, 537, 796
- Weaver, R., McCray, R., Castor, J., Shapiro, P., & Moore, R. 1977, *ApJ*, 218, 377
- Weth, C., Mészáros, P., Kallman, T., & Rees, M. J. 2000, *ApJ*, 534, 581
- Wijers, R. A. M. J., & Galama, T. J. 1999, *ApJ*, 523, 177
- Woosley, S. E. 2000, in *Fifth Huntsville Conference on Gamma-Ray Bursts*, ed. R. M. Kippen, R.S. Mallozzi, & V. Connaughton (New York: AIP), 555

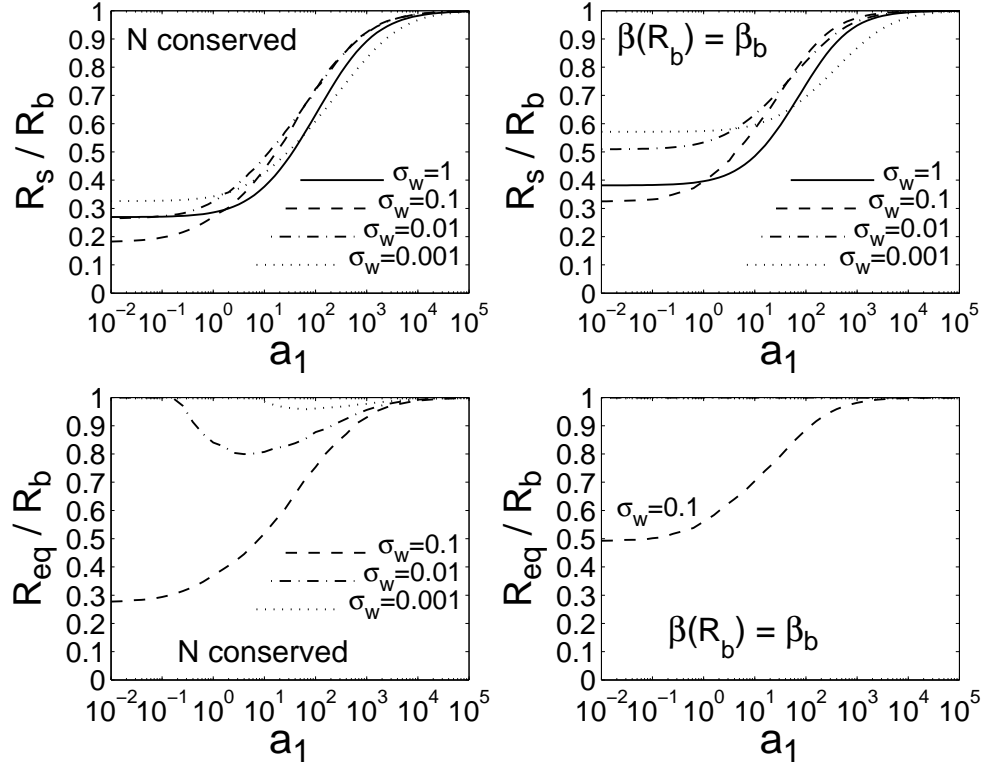


Fig. 1.— The wind-shock radius R_s (*top* panels) and the equipartition radius R_{eq} (*bottom* panels), normalized by the bubble radius R_b , as functions of the parameter a_1 (defined in eq. [43]) for 4 values of the pulsar-wind magnetization parameter σ_w . The *left* panels present solutions obtained under the particle-conservation constraint (eq. [44]), whereas the *right* panels show solutions derived by fixing the gas speed at R_b (eq. [45]).

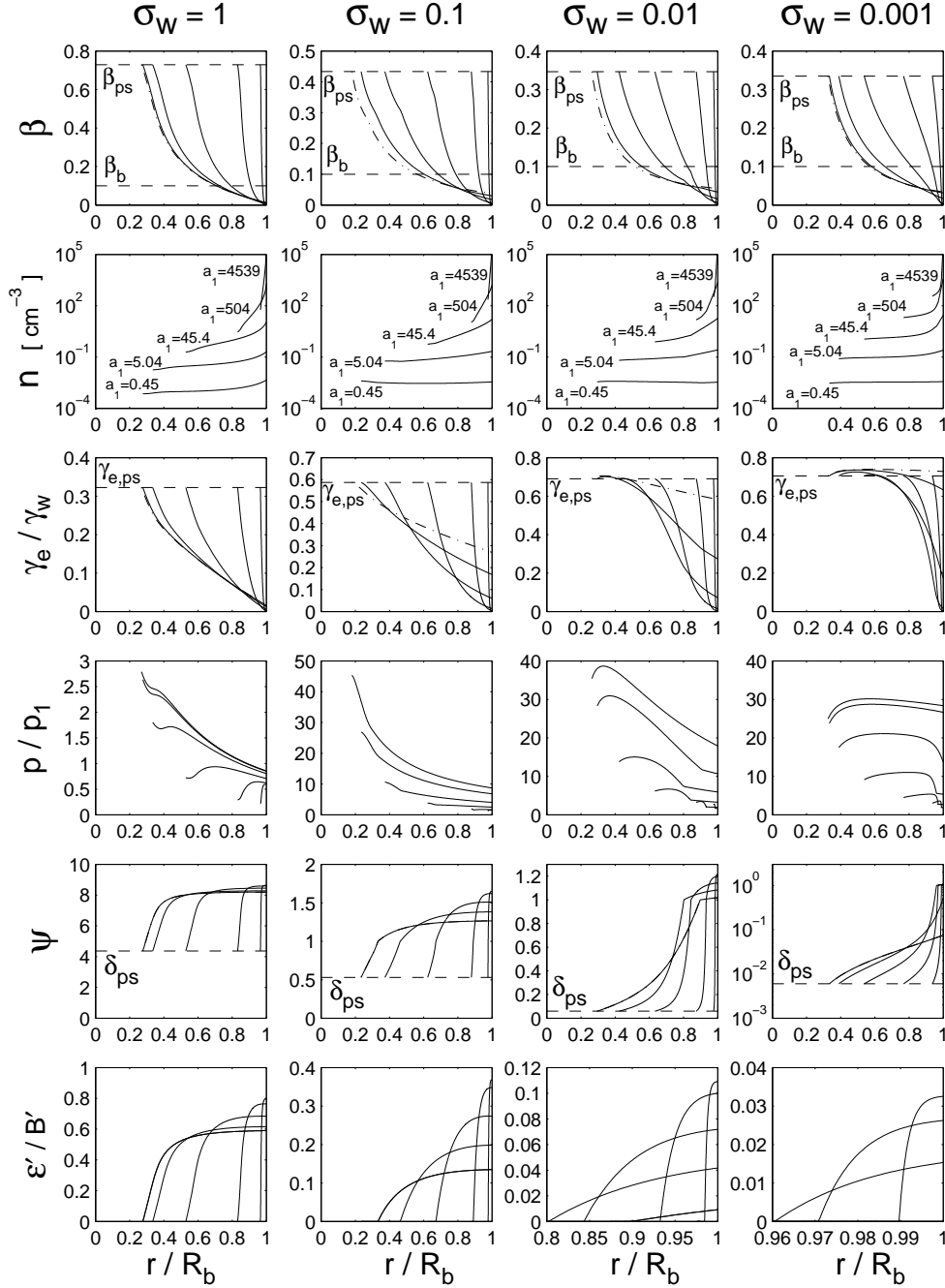


Fig. 2.— The panels show the radial distributions of β (the gas speed in units of the speed of light), n (the particle number density, for which the dimensional scaling corresponds to the fiducial values of the model parameters), γ_e (the random electron/positron Lorentz factor, normalized by the pulsar-wind Lorentz factor γ_w), p (the particle pressure, normalized by p_1 ; see eq. [37]), $\psi \equiv (1 + \mathcal{E}'/B')^2 B'^2/8\pi p$, and \mathcal{E}'/B' (the ratio of the comoving electric and magnetic fields) in the model PWBs for 4 values of the pulsar-wind magnetization parameter σ_w (listed at the top of the respective columns of panels). The solution curves in each panel correspond to 5 values of the parameter a_1 : 0.45, 5.04, 45.3, 504, and 4539 (for endpoints progressing respectively from left to right); they were obtained by imposing the particle-conservation constraint (eq. [44]).

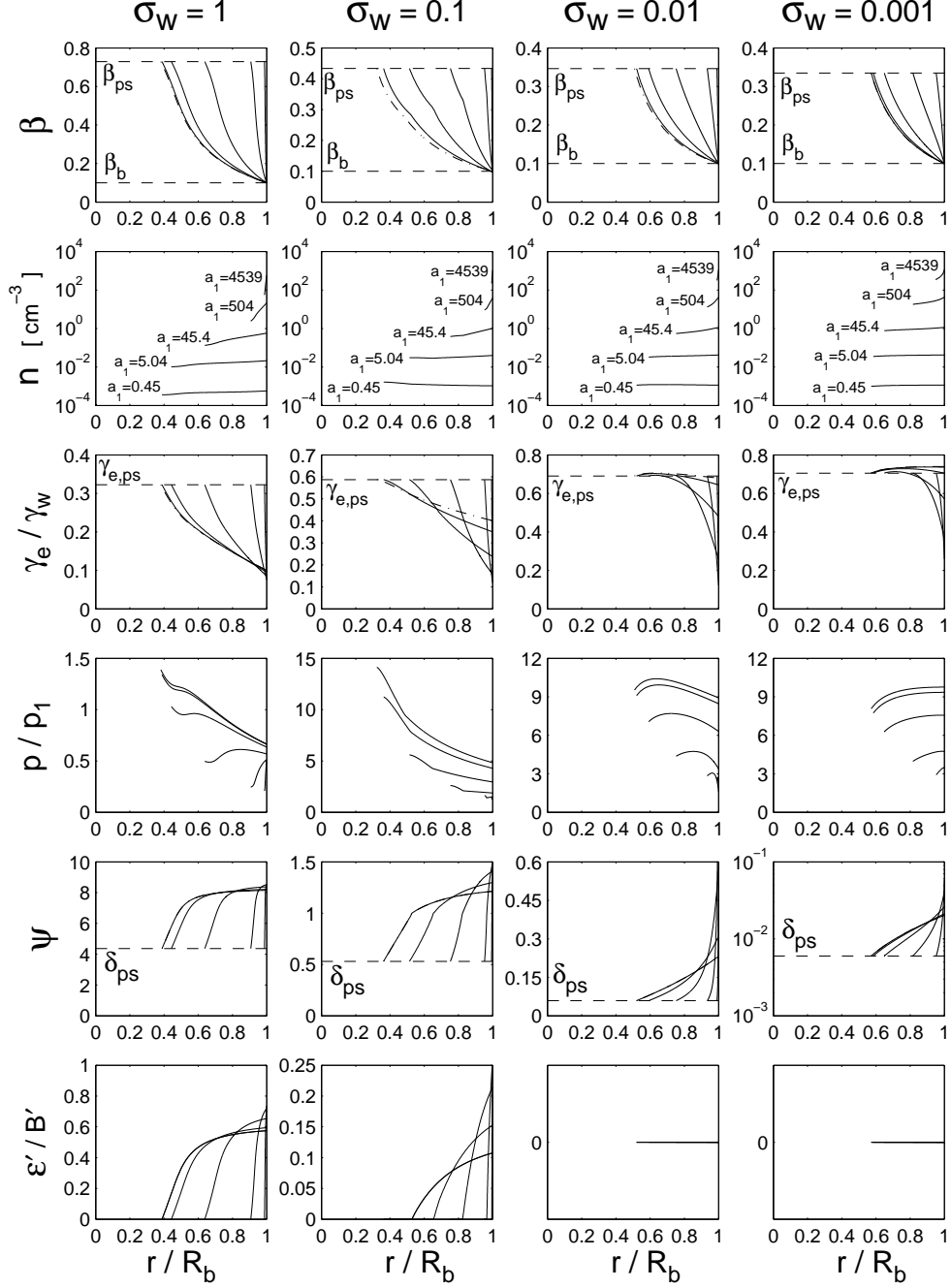


Fig. 3.— Same as Fig. 2, except that the solutions were obtained by using the final-speed constraint (eq. [45]) instead of the particle-conservation constraint.

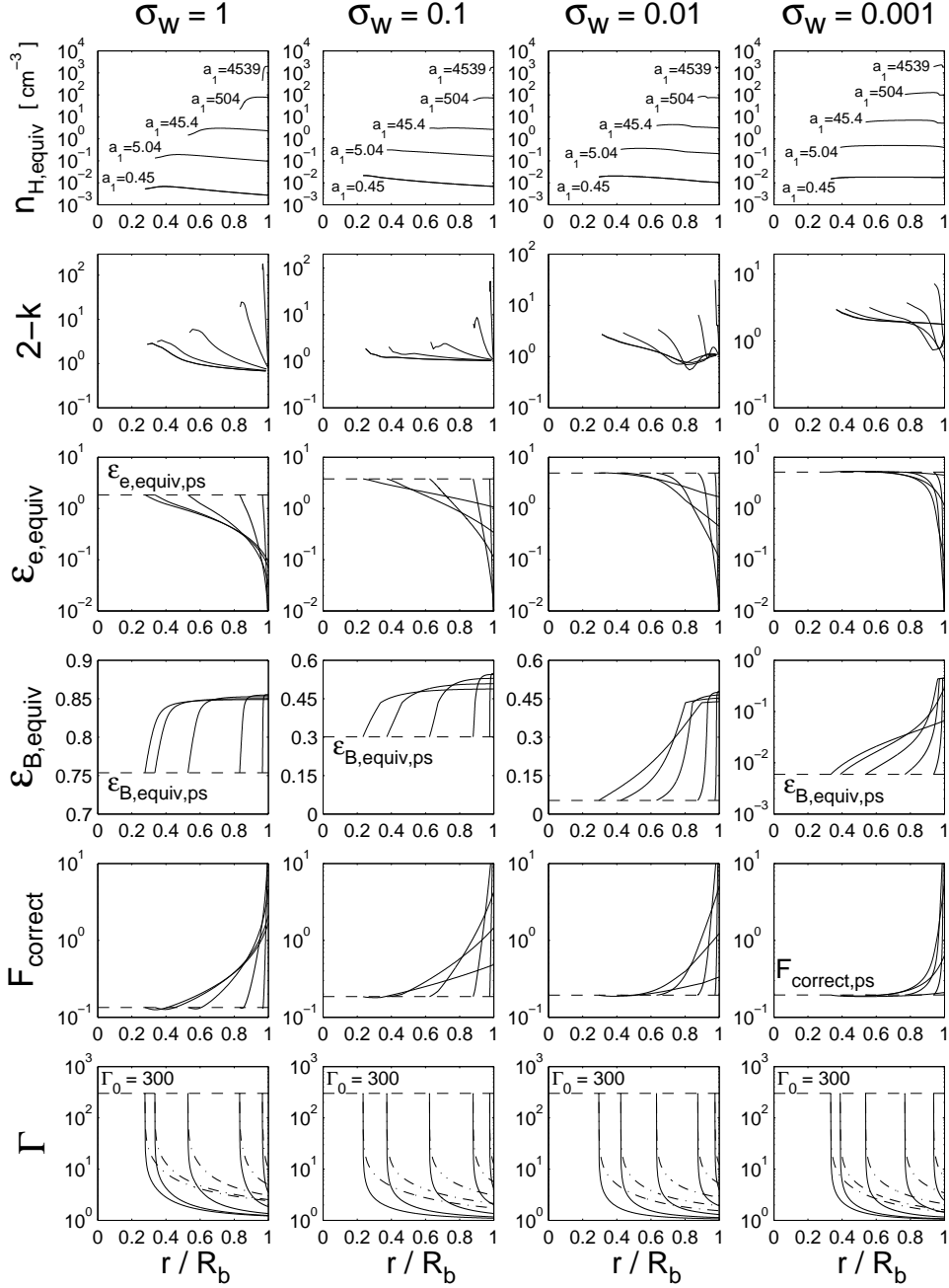


Fig. 4.— The panels show the radial distributions of $n_{\text{H,equiv}}$ (the effective hydrogen number density, eq. [51]), $2-k$ (with $k \equiv -d \log n_{\text{H,equiv}}/d \log r$ being the effective power-law index of the equivalent hydrogen density distribution), $\epsilon_{e,\text{equiv}}$ (the equivalent electron energy fraction, eq. [52]), $\epsilon_{B,\text{equiv}}$ (the equivalent magnetic energy fraction, eq. [53]), $F_{\text{correct}} = n/n_{\text{H,equiv}}$ (the flux correction factor, eq. [54]), and the Lorentz factor of the shocked bubble material (for a spherical shock driven into the PWB by an outflowing mass of energy E and initial Lorentz factor Γ_0) for the PWB solutions depicted in Fig. 2. The displayed results correspond to the fiducial values of the model parameters. The *solid* and *dash-dotted* curves in the bottom panels correspond to $E = 10^{52}$ and 10^{53} ergs, respectively.

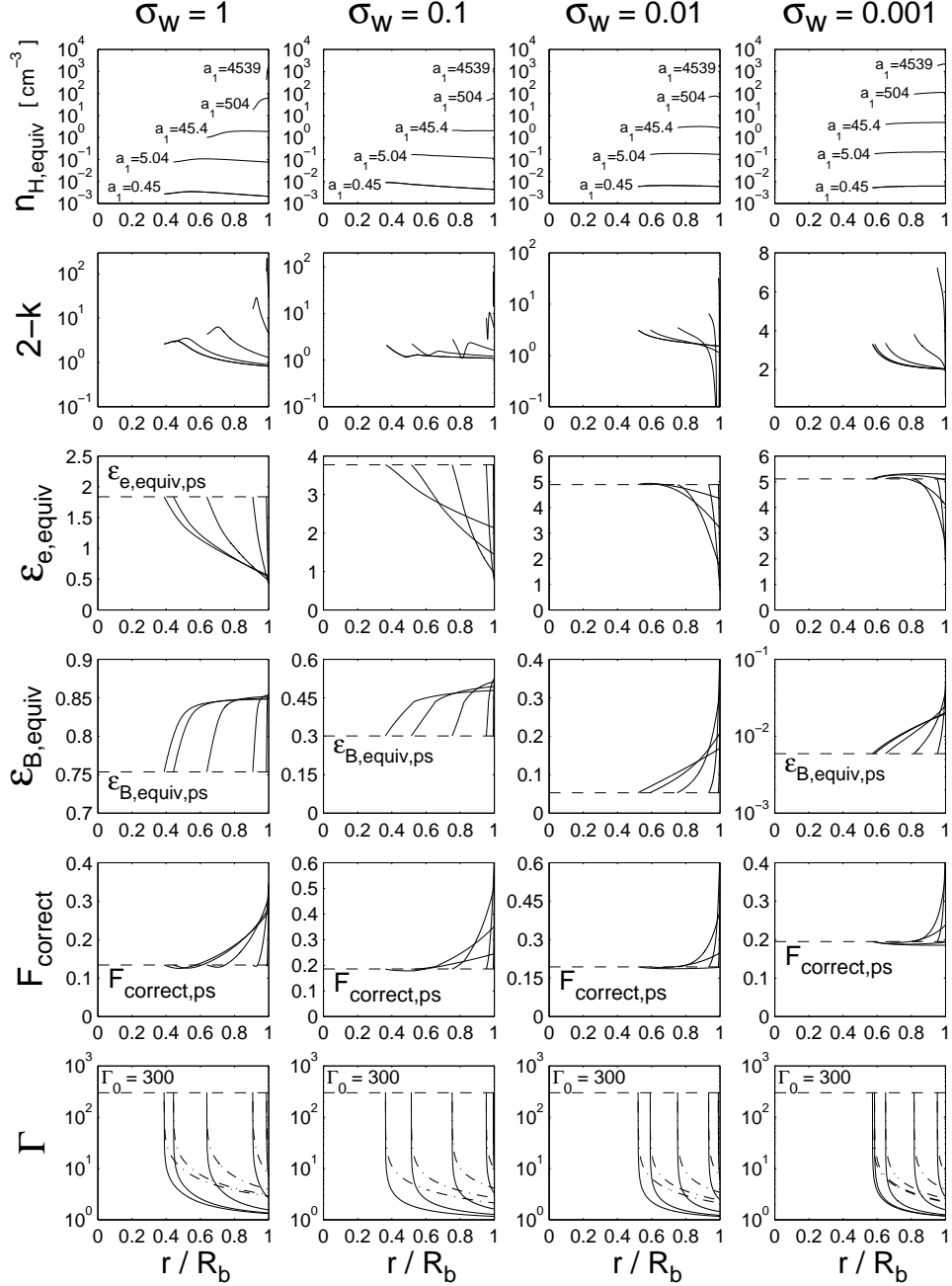


Fig. 5.— Same as Fig. 4, except that the results correspond to the PWB solutions depicted in Fig. 3.